Title

p|w PRODUCTION IN PHOTON PHOTON INTERACTIONS

Author

Derby, K.A.

Publication Date

1987-08-01

Thesis/dissertation

LBL-23548 c.2

Lawrence Berkeley Laboratory

UNIVERSITY OF CALIFORNIA

Physics Division

**$\rho^0\omega$ Production in
Photon Photon Interactions**

K.A. Derby
(Ph.D. Thesis)

August 1987

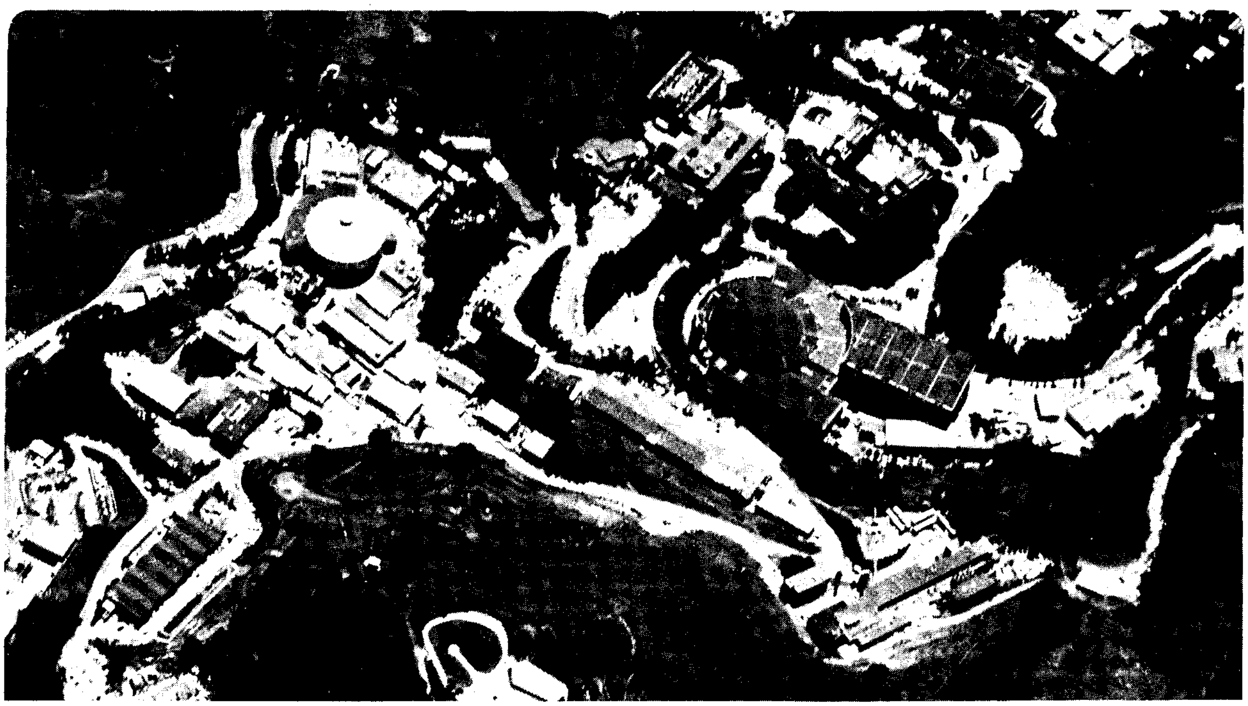

Prepared for the U.S. Department of Energy under Contract DE-AC03-76SF00098

LBL-23548

$\rho^0\omega$ Production in Photon Photon Interactions

By

Kevin Arthur Derby

Ph.D Thesis

August 2, 1987

Lawrence Berkeley Laboratory

University of California

Berkeley, CA 94720

Abstract

The subject of this dissertation is the production of the $\rho^0\omega$ final state in photon photon interactions. The production of the $\rho^0\omega$ final state has been of interest primarily because of its similarity to the related process $\gamma\gamma \rightarrow \rho^0\rho^0$. The cross section for $\rho^0\rho^0$ production demonstrates a peaking near threshold, the mechanism of which has been the subject of considerable speculation. The data sample used for the analysis was obtained using the TPC detector facility at the PEP e^+e^- storage ring and corresponds to an integrated e^+e^- luminosity of 64 pb^{-1} at 29 GeV center of mass energy. Our estimate of the $\rho^0\omega$ cross section is compared to the predictions of several models which have been used to account for the observed $\rho^0\rho^0$ cross section. The experimental results are consistent with the predictions of a threshold enhancement model as well as those of a four quark ($qq\bar{q}\bar{q}$) resonance model. However, they disagree with the predictions of a t-channel factorization approach.

This work is supported by the United States Department of Energy under Contract DE-AC03-76SF00098

Contents

Acknowledgements

First and foremost, I would like to acknowledge the efforts of those whose skill and dedication made the TPC a reality. Some of the names that come to mind in this regard are Al Clark, Mike Ronan, Margie Shapiro, Dick Kofler, Nick Hadley, Bill Gary, Phillipe Eberhard, Forest Rouse, and Gerry Lynch. I am also grateful to the people who contributed directly to the analysis in this thesis, namely Mike Ronan, Ron Ross, Gerry Lynch, Gordon VanDalen, Bill Moses, and Tony Barker. I'd like to thank my thesis committee, Ron Ross, Lynn Stevenson, and Selig Kaplan for their comments and suggestions on this dissertation.

On a more personal note, I'd like to thank Mike Ronan for being a friend as well as a teacher. It was a privilege to work with Mike, to share the late night philosophy, the early morning doughnuts, and the camaraderie that comes from total commitment to a common goal. I'd also like to thank my adviser, Ron Ross, for his gentle yet steady guidance throughout my graduate career. His confidence and support helped me to weather some difficult times, while his sound physics advice saved me months of wasted analysis effort.

I thank my sisters, my parents, Terry, Scott, and Denise for their love and support during these eight long years. Thanks also to Michael for being my dearest friend, for sharing with me the joys and disappointments of growing up over the last twelve years.

This thesis is dedicated to my love and inspiration, Kelly.

Chapter 1

Introduction

It is the rather ambitious goal of particle physicists to understand the nature of the elemental constituents of matter and the mechanisms through which these constituents interact. Current theories generally divide the particles which comprise matter into two groups, leptons and hadrons, interacting through four forces - the strong, electromagnetic, weak, and gravitational forces. The distinction between leptons and hadrons is based on the forces through which they interact; hadrons may interact via all four forces whereas leptons do not have strong interactions.

In recent years, considerable progress has been made in elucidating the nature of fundamental interactions, primarily through the development of a class of field theories known as renormalizable gauge theories. These theories have proven to be remarkably successful in describing observable phenomena. The classic example of such a theory, and indeed the basis for subsequent, more general theories, is the theory of electromagnetic interactions, Quantum Electrodynamics. This theory has been extensively tested, in some cases (as in the g factor of the electron) to a level of 1 part in 10^9, and has never been found to be in disagreement with experiment. This is remarkable achievement for any theory.

With this encouragement, QED has been extended to also describe the weak interactions [1], the resulting theory being known as the standard model of electro-weak interactions, or just the standard model. A subsequent generalization of the standard model, by incorporating Quantum Chromodynamics (QCD), accommodates the description of strong interactions and is currently the most complete theory of particle interactions. These theories, also, have enjoyed some spectacular successes, perhaps the most notable of which may be the recent discovery of the Z^0, whose existence was postulated well over a decade ago.

A common feature of gauge theories is a requirement of local gauge invariance of the Lagrangian; this requirement is met by introducing the so-called gauge boson fields. Interactions between other particles in the theory may then be viewed as being mediated by the exchange of quanta of the gauge boson fields. The photon is the gauge boson introduced to maintain the invariance of the QED Lagrangian and hence is the mediator of the electromagnetic force. The Z^0, W^+, and W^- bosons are introduced in the extension to the weak force, and finally, eight gluons are introduced in QCD to account for the color force.

As the mediators of interactions between charged particles, photons are not ordinarily thought of as interacting among themselves. Nevertheless, photons can and do interact, albeit indirectly, through quantum fluctuations of the vacuum. Such an interaction is depicted in Figure 1.1, in which two photons annihilate to produce a lepton-antilepton or quark-antiquark pair. The possibility of such interactions was realized decades ago, however photon photon collisions were not directly observed until 1970, primarily due to the limitations of experimental techniques previously available.

The study of photon photon interactions has rapidly burgeoned into a considerable field of endeavor, which will be briefly highlighted in Section 1.2 . The analysis presented in this thesis is concerned with the production of vector mesons in photon-photon interactions, or more specifically, with the process $\gamma\gamma \to \rho^0\omega$. For reasons to be outlined in Section 1.2.3, this reaction is of some interest, and

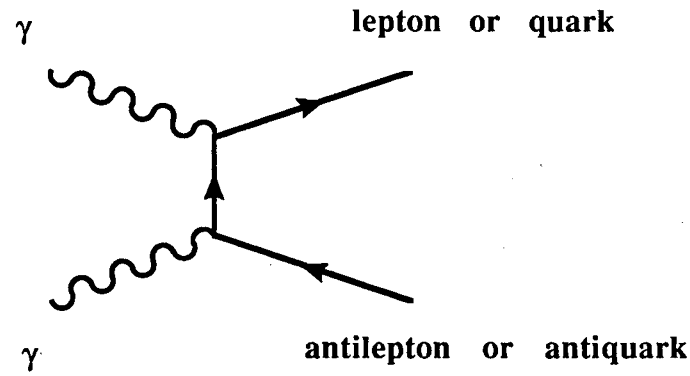

Figure 1.1: A photon-photon interaction

several efforts have been made to observe this process experimentally. The goal of this thesis, then, is to observe, and measure a cross section for, the reaction $\gamma\gamma \to \rho^0\omega$.

The presentation of this analysis is organized in the following manner. The first chapter gives an overview of the study of photon-photon interactions and the kinematics of photon-photon collisions in an electron positron storage ring. In the second chapter, the apparatus used to collect the raw data for this analysis is described. The third chapter is concerned with the process of refining the raw data and selecting $\gamma\gamma \to \rho^0\omega$ events. The procedure used for simulating detector response and reconstruction of events is described in fourth chapter. Finally, evidence for $\rho^0\omega$ production and an estimate of the cross section for this process are presented. The implications of this result are also discussed at this time.

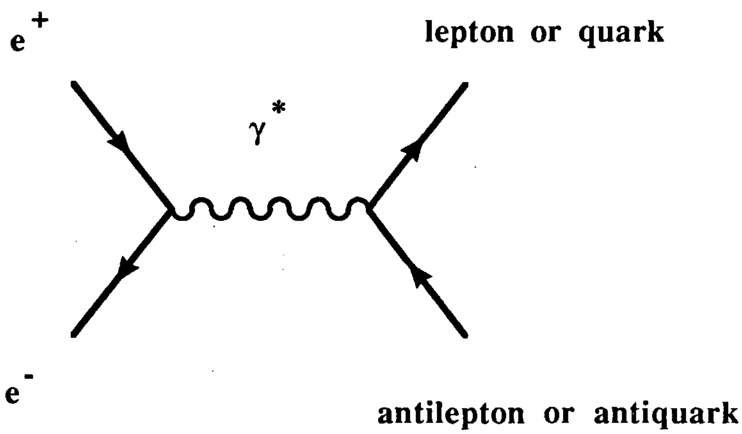

Figure 1.2: e^+e^- annihilation through one photon

1.1 Kinematics of the reaction $e^+e^- \rightarrow e^+e^-X$

The study of particle interactions in high energy physics proceeds via collisions. Early experiments involved the collision of a beam of rapidly moving particles with a stationary target, such facilities being known as fixed target machines. The introduction of circular accelerators in which counter rotating beams of particles collide, known as storage rings, allowed the attainment of much higher center of mass energies, accounting for the rapid proliferation of such machines. Storage rings which collide electrons with positrons have an additional advantage in that the initial state is comprised of particles which are very accurately pointlike and whose interactions are well understood.

Electron-positron storage rings were primarily designed to study reactions which proceed via the one photon annihilation channel depicted in Figure 1.2. In this reaction, the electron and positron annihilate, producing a virtual photon which then decays to a lepton-antilepton pair or a quark-antiquark pair. The channel in which the lepton-antilepton pair is produced provides a means of testing the current understanding of electromagnetic and weak interactions, while quark-antiquark production provides an avenue for studying, among other things, the fragmentation of quarks into observed hadrons.

Storage rings can also be used to study photon-photon interactions. The electromagnetic field of a relativistic charged particle can be regarded as a flux of virtual photons, hence the observation of photon-photon collisions in e^+e^- storage rings via the diagram of Figure 1.3 . The kinematics of this reaction are developed below.

The incident electron and positron have four momenta p_1 and p_2 respectively, while the scattered electron and positron have momenta p_1' and p_2'. In the case of unpolarized beams (as in this experiment) there is no overall azimuthal dependence, therefore only five variables are needed to specify the $\gamma\gamma$ system. A convenient choice of variables is the set $(E_1', E_2', \theta_1, \theta_2, \phi)$, where ϕ is the angle between the lepton scattering planes. The squared invariant masses of the photons are then

$$q_i^2 = 2m_e^2 - 2E_{beam}E_i'\{1 - \cos\theta_i\sqrt{1-(m_e/E_{beam})^2}\sqrt{1-(m_e/E_i')^2}\} \qquad (1.1)$$

Defining the quantity $Q_i^2 = -q_i^2$, equation 1.1 may be approximated as (in the case where $E_{beam}, E_i' \gg m_e$)

$$Q_i^2 \simeq 4E_{beam}E_i'\sin^2(\theta_i/2) \qquad (1.2)$$

The center of mass energy of the $\gamma\gamma$ system, denoted $W_{\gamma\gamma}$, is

$$W_{\gamma\gamma}^2 = (q_1 + q_2)^2 = \text{invariant mass of final state X} \qquad (1.3)$$

A few general features of the two photon process can be noted. The energies of the emitted photons can be anywhere in the range $0 - E_{beam}$, so $W_{\gamma\gamma}$ can

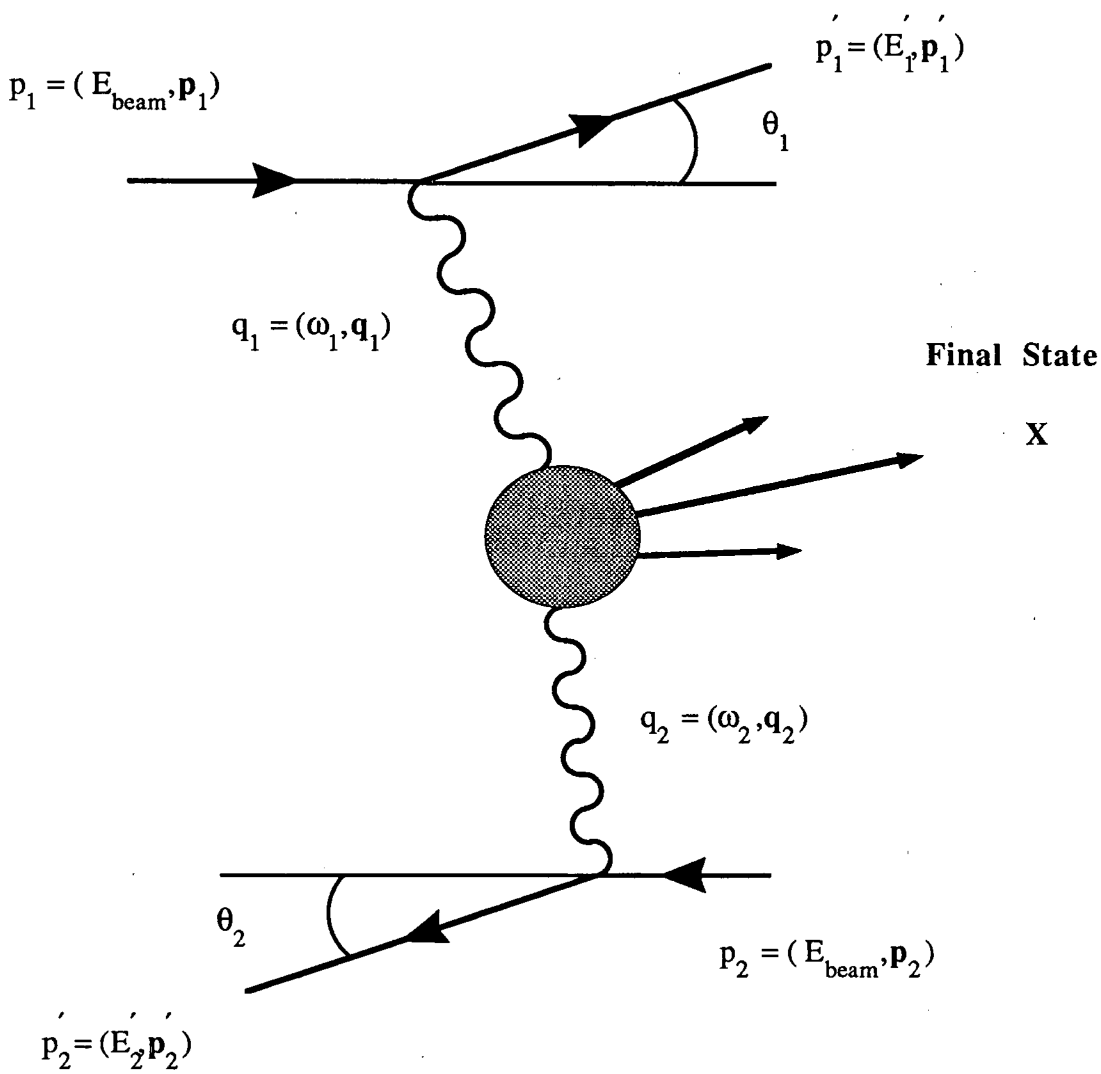

Figure 1.3: Two photon interaction in an e^+e^- collider

take any value from 0 to $2E_{beam}$. Due to the photon propagators in the matrix element for this process (to be discussed further below), the Q^2 spectrum of the photons will be strongly peaked at 0. Thus, most photons will be nearly real, and the momenta of both the scattered electrons and the photons will tend to be along the beam direction. This means that the $\gamma\gamma$ system will in general have a small momentum component transverse to the beam line. Experimentally, the scattered electrons are known as tags if they are detected, hence the events are categorized as no tag, single tag, or double tag, depending on the number of scattered electrons detected in the final state. The analysis presented herein is a no tag analysis, i.e. neither of the scattered electrons need be detected. In fact, since events with a large q^2 tag will eventually be discarded by momentum balance requirements in the event selection, this analysis is, in some sense, an anti-tag analysis. Finally, since the energies of the photons are in general unequal, the $\gamma\gamma$ system will usually have some momentum along the beam line, unlike one photon annihilation events.

1.1.1 The Luminosity Function

The photon-photon cross section is derived from the measurement of two quantities: the number of photon-photon interactions and the photon flux, or luminosity. In an e^+e^- storage ring, the flux of photons available for interaction must be derived from the measured e^+e^- luminosity (which for this experiment was determined by monitoring the rate of Bhabha events). The cross sections for $e^+e^- \to e^+e^-\gamma\gamma \to e^+e^-X$ and $\gamma\gamma \to X$ are related through

$$\sigma_{e^+e^- \to e^+e^- X} = \mathcal{L}_{\gamma\gamma}\sigma_{\gamma\gamma \to X} \tag{1.4}$$

where $\mathcal{L}_{\gamma\gamma}$, the luminosity function, is essentially a number relating the e^+e^- luminosity to the $\gamma\gamma$ luminosity, and is completely calculable in QED. A brief development of the luminosity function is presented below, but more complete treatments can be found in, for instance, [2] or [3].

The transition matrix element for the process of Figure 1.3 is written as

$$\mathcal{M} = e^4[\frac{1}{q_1^2 q_2^2}][\bar{u}(p_1', \sigma_1')\gamma^\mu u(p_1, \sigma_1)][\bar{v}(p_2', \sigma_2')\gamma^\nu v(p_2, \sigma_2)]A^X_{\mu\nu} \tag{1.5}$$

The first term in brackets is from the two photon propagators, the second and third terms represent the lepton-photon vertices and the last term describes the coupling of the two photons to the final state X. The differential cross section is then

$$d\sigma_{e^+e^-\to e^+e^-X} = \frac{\alpha^2}{64\pi^4 E^2_{beam} q_1^2 q_2^2}\{\rho_1^{\mu\nu}\rho_2^{\mu'\nu'}\}M^X_{\mu\nu\mu'\nu'}\frac{d^3\vec{p}_1' d^3\vec{p}_2'}{E_1' E_2'} \tag{1.6}$$

where the density matrices for the photons are given by

$$\rho_i^{\mu\nu} = -\frac{q_i^2 g^{\mu\nu} + 2(p_i'^\mu p_i^\nu + p_i^\mu p_i'^\nu)}{q_i^2} \tag{1.7}$$

and the tensor describing the production of the state X is

$$M^X_{\mu\nu\mu'\nu'} = 8\pi^2 \int A^X_{\mu\nu} A^X_{\mu'\nu'}\delta(q_1 + q_2 - P_X)d\Gamma_X \tag{1.8}$$

Here P_X is the four-momentum of the final state X and the integral is over the final state phase space, Γ_X.

The tensor $M^X_{\mu\nu\mu'\nu'}$ has 256 components, however the requirements of Lorentz invariance and current conservation can be used to show that only 10 are independent. Time reversal invariance implies that two of these are 0, and in the case of unpolarized beams two more vanish. Working in the helicity basis described in [2], the differential cross section becomes

$$\begin{aligned} d\sigma_{e^+e^-\to e^+e^-X} &= \frac{\alpha^2\sqrt{(q_1 q_2)^2 - q_1^2 q_2^2}}{32\pi^4 E^2_{beam} q_1^2 q_2^2}\{\frac{d^3\vec{p}_1' d^3\vec{p}_2'}{E_1' E_2'}\} \\ &\times\{4\rho_1^{++}\rho_2^{++}\sigma_{TT} + 2\rho_1^{++}\rho_2^{00}\sigma_{TL} + 2\rho_1^{00}\rho_2^{++}\sigma_{LT} + \rho_1^{00}\rho_2^{00}\sigma_{LL} \\ &+2\mid \rho_1^{+-}\rho_2^{+-}\mid \tau_{TT}cos(2\tilde{\phi}) - 8\mid \rho_1^{+0}\rho_2^{+0}\mid \tau_{TL}cos(\tilde{\phi})\} \end{aligned} \tag{1.9}$$

The σ's and τ's are the cross sections for $\gamma\gamma \to X$ in the case of transverse photons (T) or longitudinal photons (L). Since real photons can have only a transverse polarization, all terms with a L subscript vanish as $Q_i^2 \to 0$. Furthermore if one integrates over the angle between the lepton scattering planes in the $\gamma\gamma$ CMS, $\tilde{\phi}$, the term containing τ_{TT} vanishes. Therefore, for no-tag studies the σ_{TT} term will dominate and the differential cross section can be approximated by

$$d\sigma_{e^+e^-\to e^+e^-X} = \frac{\alpha^2\sqrt{(q_1q_2)^2 - q_1^2q_2^2}}{32\pi^4 E_{beam}^2 q_1^2 q_2^2}\frac{d^3\vec{p}_1' d^3 p_2'}{E_1' E_2'}[4\rho_1^{++}\rho_2^{++}\sigma_{TT}(W_{\gamma\gamma}, q_1^2, q_2^2)] \quad (1.10)$$

Putting this in terms of the luminosity function, $\mathcal{L}_{\gamma\gamma}^{TT}$, with the superscript indicating the transverse photon approximation, this becomes

$$\frac{d^5\sigma_{e^+e^-\to e^+e^-X}}{d\omega_1 d\omega_2 d\theta_1 d\theta_2 d\phi} = \frac{d^5\mathcal{L}_{\gamma\gamma}^{TT}}{d\omega_1 d\omega_2 d\theta_1 d\theta_2 d\phi}\sigma_{TT}(W_{\gamma\gamma}, q_1^2, q_2^2) \quad (1.11)$$

The differential luminosity function is given by

$$\frac{d^5\mathcal{L}_{\gamma\gamma}^{TT}}{d\omega_1 d\omega_2 d\theta_1 d\theta_2 d\phi} = \frac{4\alpha^2}{16\pi^3 E_{beam}^2}\frac{E_1' E_2'}{q_1^2 q_2^2}\sqrt{U}\rho_1^{++}\rho_2^{++} \quad (1.12)$$

with the density matrix elements being

$$\rho_1^{++} = \frac{(2p_1q_2 - q_1q_2)^2}{2U} + \frac{1}{2} + 2\frac{m_e^2}{q_1^2} \quad (1.13)$$

$$\rho_2^{++} = \frac{(2p_2q_1 - q_1q_2)^2}{2U} + \frac{1}{2} + 2\frac{m_e^2}{q_2^2} \quad (1.14)$$

the quantity U being defined by $U = (q_1q_2)^2 - q_1^2q_2^2$.

The differential luminosity function can be integrated numerically to find its dependence on $W_{\gamma\gamma}$. The resulting function, $d\mathcal{L}_{\gamma\gamma}^{TT}/dW_{\gamma\gamma}$, is plotted in Figure 1.4 for the case of $E_{beam} = 14.5$. The e^+e^- and $\gamma\gamma$ cross sections in a given $W_{\gamma\gamma}$ range are then related by

$$\sigma_{e^+e^-\to e^+e^-X} = \sigma_{\gamma\gamma\to X}\int \frac{d\mathcal{L}_{\gamma\gamma}^{TT}}{dW_{\gamma\gamma}} dW_{\gamma\gamma} \quad (1.15)$$

1.1.2 The Equivalent Photon Approximation

Another approximation which often useful for no-tag studies is the Equivalent Photon Approximation. This approach derives its name from the realization

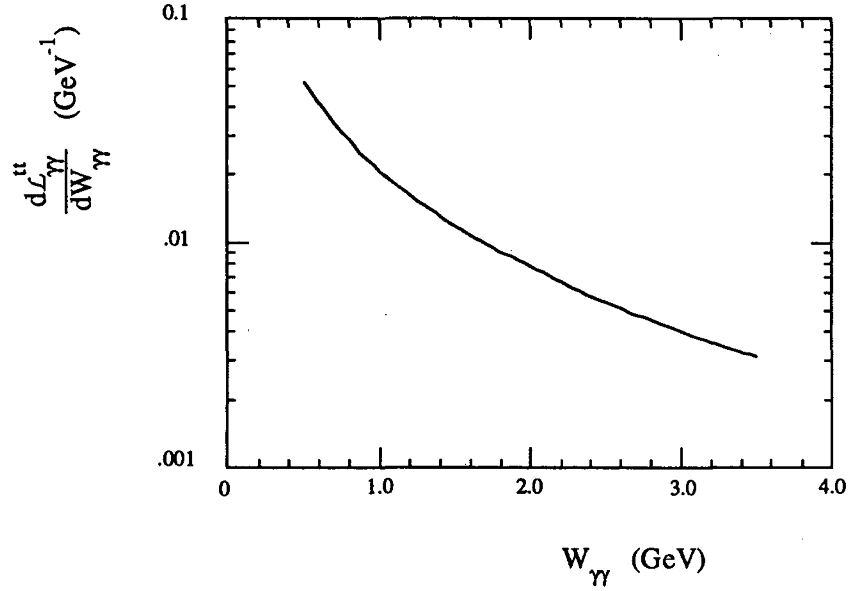

Figure 1.4: $d\mathcal{L}^{TT}_{\gamma\gamma}/dW_{\gamma\gamma}$ as a function of $W_{\gamma\gamma}$

by Fermi, in 1924, that the field of a fast charged particle is similar to a flux of photons distributed in energy with according to some spectrum $N(\omega)$. Expressing the differential cross section as (see the development in [4])

$$\begin{aligned} d\sigma_{e^+e^-\to e^+e^-X} &= \frac{\alpha^2}{2}\frac{1}{E^2_{beam}}\int\frac{d^3\vec{p}_1'}{E_1'}\int\frac{d^3\vec{p}_2'}{E_2'}(\frac{1}{q_1^2q_2^2})^2(2p_1^\mu p_1^\nu+\frac{1}{2}q_1^2g^{\mu\nu}) \\ &\times(2p_2^\alpha p_2^\beta+\frac{1}{2}q_2^2g^{\alpha\beta})M^\dagger_{\mu\alpha}M_{\nu\beta}\delta(q_1+q_2-P_X)d\Gamma_X \quad (1.16) \end{aligned}$$

the EPA result is found by: 1) performing the photon polarization sums in the Coulomb gauge, 2) retaining only the transverse current contribution, and 3) approximating the transverse current and the phase space factor by their values at $q_1^2 = q_2^2 = 0$. Integrating over azimuthal angles and integrating the electron scattering angles up to θ_{max}, the maximum angle through which an electron can scatter and not be detected, the cross section is approximated by

$$d\sigma_{e^+e^-\to e^+e^-X} \simeq \int\frac{d\omega_1}{\omega_1}\int\frac{d\omega_2}{\omega_2}N(\omega_1,\theta_{max})N(\omega_2,\theta_{max})d\sigma_{\gamma\gamma\to X}(\omega_1,\omega_2) \quad (1.17)$$

where the spectrum $N(\omega, \theta_{max})$ is given by

$$\begin{aligned} N(\omega,\theta_{max}) &= \frac{\alpha}{\pi}\{\frac{E_{beam}^2+E'^2}{E_{beam}^2}(\ln\frac{E_{beam}\theta_{max}}{2m_e}-\frac{1}{2})+\frac{(E_{beam}-E')^2}{2E_{beam}^2}(\ln\frac{2E'}{E_{beam}-E'}+1) \\ &\quad +\frac{(E_{beam}+E')^2}{2E_{beam}^2}\ln\frac{2E'}{\sqrt{(E_{beam}-E')^2+E_{beam}E'\theta_{max}^2}}\} \end{aligned} \tag{1.18}$$

This simple relation lends itself to Monte Carlo applications, moreover, it reproduces most of the kinematic features of the $\gamma\gamma$ collision process mentioned in the previous section. This subject will be discussed further in Chapter 4.

1.2 Photon Photon Interactions

The field of two photon physics, though still very young, has expanded in many different directions. While it is far beyond the scope of this presentation to attempt to review the subject in any sort of depth, there are several review articles [5,2] which can provide a good introduction to the subject. In order to impart a flavor of the current state of two photon physics, a few of the topics which have been of recent interest are mentioned in the following sections.

1.2.1 Meson Production

In the quark-parton picture, mesons are bound states of quark-antiquark pairs. These states are assigned to locations in the octet and singlet representations of the $SU(3)$ group according to the decomposition

$$3 \otimes \bar{3} = 8 \oplus 1 \tag{1.19}$$

The two photon production of a meson is illustrated in Figure 1.5, in which the photons annihilate forming a quark and antiquark, which are then bound in a meson. If the two photons are real, or nearly so, the Yang-Landau theorem implies that only mesons from the pseudoscalar or tensor nonets can be produced. The flavor neutral members of these nonets are expressed as admixtures of the

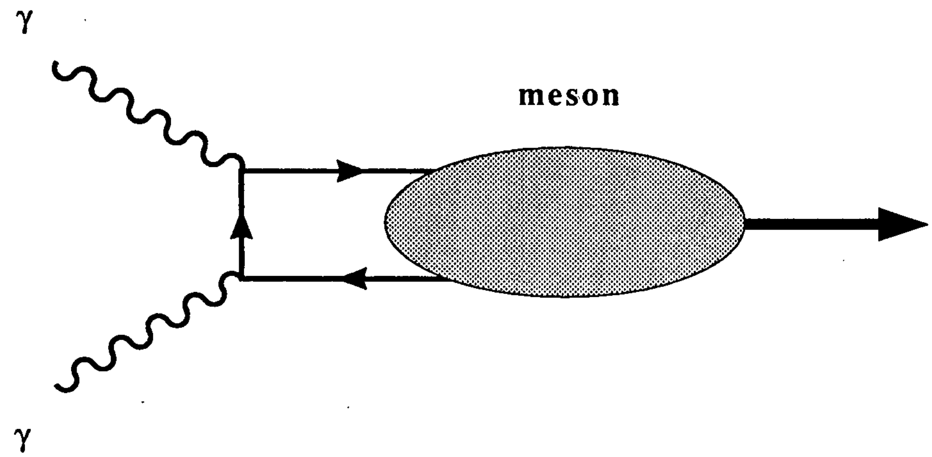

Figure 1.5: Meson production by two photons

u,d, and s quarks by

$$
\begin{aligned}
|\pi^0\rangle(|A_2\rangle) &= \frac{|d\bar{d}\rangle - |u\bar{u}\rangle}{\sqrt{2}} \\
|\eta_8\rangle(|f_8\rangle) &= \frac{|d\bar{d}\rangle + |u\bar{u}\rangle - 2|s\bar{s}\rangle}{\sqrt{6}} \\
|\eta_1\rangle(|f_1\rangle) &= \frac{|d\bar{d}\rangle + |u\bar{u}\rangle + |s\bar{s}\rangle}{\sqrt{3}}
\end{aligned} \tag{1.20}
$$

where the members of the tensor nonet are in parentheses. Because the mass of the s quark is significantly larger than that of the u or d quarks [6,7], the $SU(3)$ symmetry is broken, and the physically observable states are mixtures of the $SU(3)$ singlet and octet states

$$
\begin{aligned}
|\eta\rangle &= \cos\Theta|\eta_8\rangle - \sin\Theta|\eta_1\rangle \\
|\eta'\rangle &= \sin\Theta|\eta_8\rangle + \cos\Theta|\eta_1\rangle \\
|f'\rangle &= \cos\Theta|f_8\rangle - \sin\Theta|f_1\rangle \\
|f\rangle &= \sin\Theta|f_8\rangle - \cos\Theta|f_1\rangle
\end{aligned} \tag{1.21}
$$

where Θ is known as the mixing angle. Since the photon couples only to electric charge, measuring the width $\Gamma(\gamma\gamma \rightarrow meson)$ is a clean way to probe the charge structure of mesons. Knowing the quark charges, this yields information about the mixing angle which can be compared to predictions from other sources, e.g. the Gell-Mann Okubo mass formula.

Observation of the two photon production of mesons can also help in the determination of a meson's spin-parity assignment. As mentioned above, two real photons cannot produce a spin 1 meson. However, if one of the photons is highly virtual, such production becomes possible. Thus, the observation of meson production in single tag studies with no corresponding production in the no tag channel helps to discriminate between spin hypotheses.

Another topic of recent interest is the search for 'glueballs', or bound states of gluons. Such objects are expected in QCD due to the non-Abelian nature of the theory. The copious production of the $\iota(1450)$ in radiative J/ψ decay makes it a likely glueball candidate since this decay is dominated in perturbation theory by the process $J/\psi \rightarrow \gamma + 2\, gluons$. Since gluons have no electric charge they cannot couple directly to photons, hence measuring the $\gamma\gamma$ width of the ι is a sensitive test of its gluonic content.

1.2.2 Deep Inelastic Lepton-Photon Scattering

Some of the strongest supporting evidence for the quark parton model came from the deep inelastic lepton-nucleon scattering experiments of the late 1960's and early 1970's. In these experiments high energy electrons were observed to scatter off nucleons in the process illustrated by Figure 1.6 . Because of the asymptotic freedom of QCD, the strong coupling constant becomes small at large momentum transfers, and the effects of strong interactions become negligible. Thus, in a scattering process with large momentum transfer the pointlike nature of the

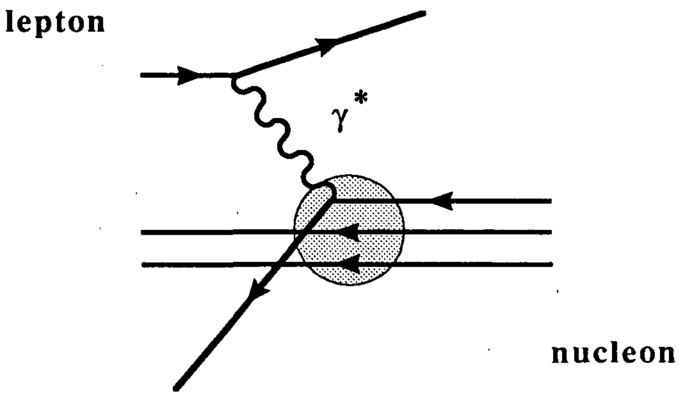

Figure 1.6: Deep inelastic lepton nucleon scattering

nucleon's constituents can be observed.

A rather similar situation is found in single tag $\gamma\gamma$ analyses. Again, a lepton scatters at a large angle, emitting a highly virtual photon suitable for probing the inner structure of a target. In this case, however, the target is not a nucleon, but a photon. The pointlike structure of the photon may be observed in a process like that of Figure 1.7, where, in the limit of large momentum transfers, the quarks are essentially free.

However, the picture is somewhat clouded due to the hadronic nature of the photon. According to the Vector Dominance Model [8], or VDM, photons which are nearly on shell are expected to behave like hadrons in their interactions. In this phenomenological picture, photons interact hadronically by turning into a virtual vector meson (ρ^0,ϕ, or ω) which then undergoes a hadronic interaction. This model has proven quite successful in describing the features of photon-

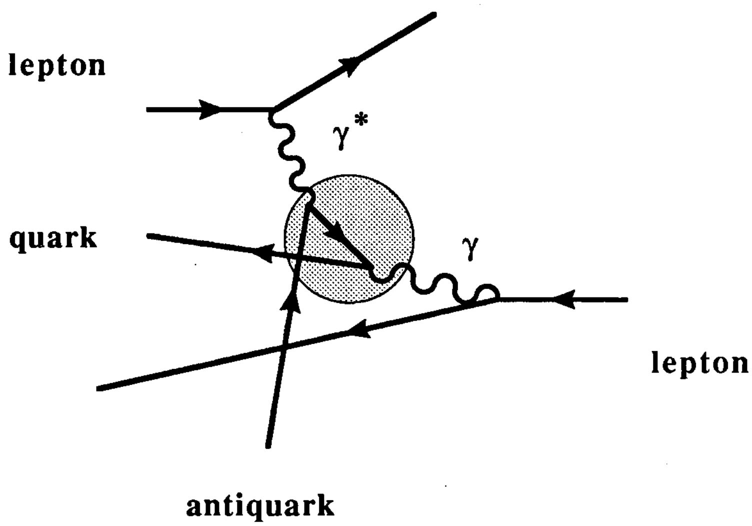

Figure 1.7: Pointlike lepton photon scattering

hadron interactions. According to VDM, the scattering process would look more like Figure 1.8, in which the virtual photon is probing, as in the case of lepton-nucleon scattering, a hadronic structure.

Experiment seems to indicate that, in fact, the photon does have this dual nature [5]. In addition it is believed that the contribution of the pointlike component to this process can be calculated in QCD, and can provide an avenue for determining the QCD scale parameter, Λ. Unfortunately, the separation of the pointlike and hadronic contributions, together with the difficulties involved with QCD calculations, have made this a difficult endeavor.

1.2.3 Hadron Production in the VDM Model

The production of hadrons in the two photon process, like deep inelastic lepton-nucleon scattering, can be visualized within both the QCD and VDM frameworks. According to QCD, hadron production would proceed according to the diagram

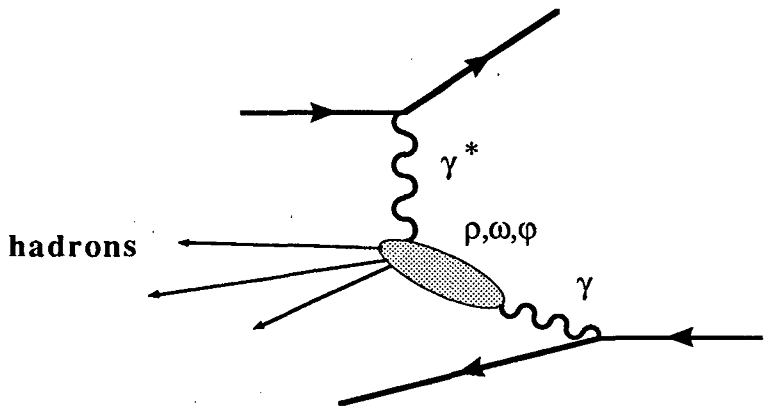

Figure 1.8: VDM lepton photon scattering

of Figure 1.9, wherein photons first couple to a quark-antiquark pair and the $q\bar{q}$ system subsequently fragments to the final state hadrons actually observed.

When the momentum transfer is small, the final state quark and antiquark will interact through gluon exchange, obscuring the pointlike photon-quark coupling. In this case the situation is perhaps better described by the VDM picture, which would view the scattering essentially as the scattering of two vector mesons. In the VDM model, the photon is expected to interact primarily as a ρ^0, less frequently as a ϕ, and least often as an ω, according to the ratio $\rho^0 : \phi : \omega = 1 : 2/9 : 1/9$. These ratios are derived from the coupling of the photon to the different charge structures of the vector mesons. Therefore, the production of for instance, a $\rho^0\rho^0$ final state, might be expected to look like the $\rho^0\rho^0$ elastic scattering of Figure 1.10 .

Perhaps the only major surprise in the field of two photon physics came in

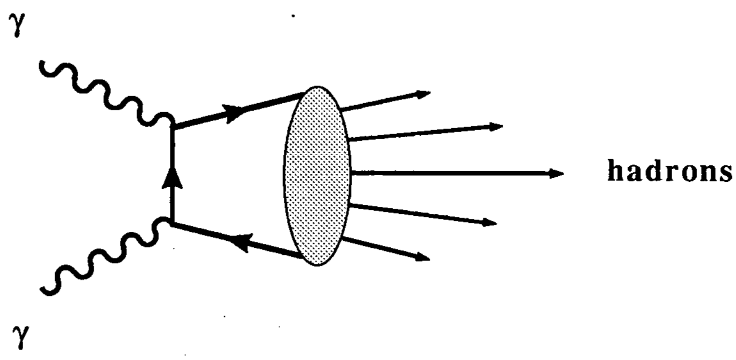

Figure 1.9: Pointlike hadron production

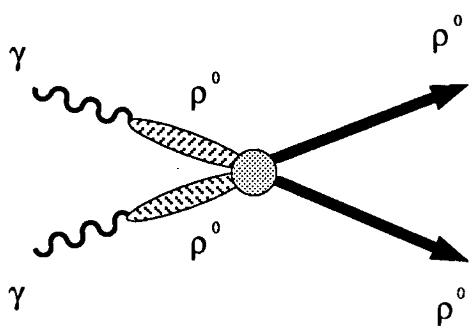

Figure 1.10: $\rho^0\rho^0$ production in VDM

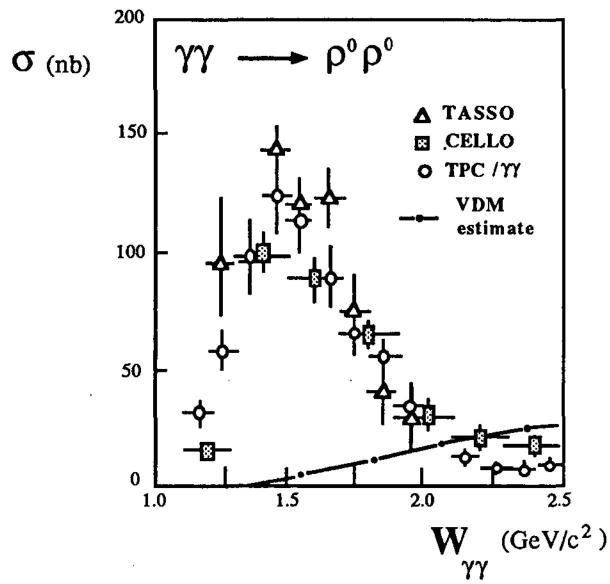

Figure 1.11: Recent measurements of the $\rho^0\rho^0$ cross section

1980 with the TASSO [9] measurement of the $\gamma\gamma \to \rho^0\rho^0$ cross section. The cross section was found to be peaked at threshold, in contrast to predictions from VDM arguments. Subsequent measurements have confirmed this behavior; Figure 1.11 shows some recent measurements, together with a prediction based on VDM arguments and an extrapolation of higher energy hadronic scattering behavior.

The observation of this peaking at threshold prompted a rash of theoretical speculation and experimental investigations. While several approaches have been taken to explain the $\rho^0\rho^0$ cross section, the most popular approach seems to be that of postulating some sort of intermediate state resonance. However, such approaches must also account for the fact that the $\gamma\gamma \to \rho^+\rho^-$ cross section is experimentally much less than the $\rho^0\rho^0$ cross section. If the proposed resonance has isospin 0, one would expect $\sigma_{\gamma\gamma\to\rho^+\rho^-} = 2\sigma_{\gamma\gamma\to\rho^0\rho^0}$ whereas for a resonance of isospin 2 one would expect $\sigma_{\gamma\gamma\to\rho^+\rho^-} = 1/2\sigma_{\gamma\gamma\to\rho^0\rho^0}$. For this reason, resonance models for the $\rho^0\rho^0$ threshold enhancement are generally limited to those which use interference between isoscalar and isotensor states to suppress the $\rho^+\rho^-$ cross section. Assuming ρ^0 dominance for both photons, isospin arguments show that such amplitudes should interfere as [41]

$$\begin{aligned} A(\rho^0\rho^0 \to \rho^0\rho^0) &= \frac{2}{3}A_{isotensor} + \frac{1}{3}A_{isoscalar} \\ A(\rho^0\rho^0 \to \rho^+\rho^-) &= \frac{\sqrt{2}}{3}A_{isotensor} - \frac{\sqrt{2}}{3}A_{isoscalar} \end{aligned} \tag{1.22}$$

if the reaction proceeds through an isoscalar and an isotensor resonance. The proposed intermediate states range from standard quark model resonances to four quark states, or even glueballs. To date, there has been no compelling evidence to select any one of the many proposed explanations for the observed $\rho^0\rho^0$ cross section.

Most of these explanations also make predictions regarding the production of other vector meson pairs, in particular, the production of the $\rho^0\omega$ final state. This process, which will be seen most often as a $\pi^+\pi^-\pi^+\pi^-\pi^0$ final state via the decays $\rho^0 \to \pi^+\pi^-$, $\omega \to \pi^+\pi^-\pi^0$, has been the subject of several experimental investigations. Until a recent preliminary result from the ARGUS collaboration [10], no evidence for the production of a $\rho^0\omega$ final state had been observed. In Chapter 5 evidence for the observation of this process will be presented. An estimate of the cross section, which serves as a test of various theoretical predictions, will also be discussed.

Chapter 2

Detector

In the effort to probe deeper into the structures of 'elementary' particles, experimental energy, size, and cost have risen dramatically over the past decade. The rather formidable experimental apparatus used to collect the data for this analysis consists of essentially two elements; an accelerator which provides high energy collisions, and a detector which identifies and tracks the products of such collisions. This chapter contains a brief description of the accelerator facility, and a somewhat more detailed description of the detector.

2.1 The PEP Facility

The data used for this analysis were collected at the PEP (Positron Electron Project) storage ring at the Stanford Linear Accelerator Center. The 3 km linear accelerator takes electrons from an electron gun and accelerates them using a series of 240 microwave cavities, or klystrons. Positrons are obtained by directing the electron beam at a target one third of the way down the accelerator, collecting the produced positrons, and then accelerating them in the same manner as the electrons. For injection into the PEP ring, electrons and positrons are accelerated to an energy of 14.5 GeV.

The PEP ring, which is 2.2 km in circumference, contains counter rotating beams of electrons and positrons. PEP is actually hexagonal in shape, consisting of six straight sections connected by six curved sections through which the particles are guided by magnetic steering fields. The average loss of 27 MeV per particle per revolution from synchrotron radiation is compensated by klystrons which keep the beams at the nominal 14.5 GeV per particle. The electrons and positrons are each gathered into three bunches, leading to collisions occurring every 2.45 μs at six interaction regions around the ring. Five of these regions house large detector systems, while the sixth is used for beam studies. Typical operating luminosities at the PEP ring are in the range $10^{30} - 10^{31}\ cm^{-2}s^{-1}$.

2.2 The PEP4/9 Detector

The PEP4/9 detector system is comprised of two major subsystems: the central detector and the forward detectors. Figure 2.1 shows a cutaway view of the central detector and one of the forward detectors, while Figure 2.2 and Figure 2.3 depict more detailed longitudinal sections of the detector system. Tables 2.1 and 2.2 summarize the characteristics of the central and forward detectors respectively (taken from [16]).

The forward detectors track particles which are emitted at very small angles from the beam line, hence they are primarily used for single and double tag two photon physics. Emphasis is therefore placed on identifying and measuring the momenta of scattered electrons from two photon events. The tracking components consist of a Čerenkov counter, a set of five planar drift chambers, a time of flight scintillator hodoscope, a calorimeter system using NaI crystals at small angles in conjunction with a lead scintillator sandwich at larger angles, and three layers of drift chambers interspersed with iron for muon identification.

It is the responsibility of the central detector to identify and measure the momenta of particles which are produced at larger angles from the beam line. Most of the components of the central detector are 'barrel' components, i.e.

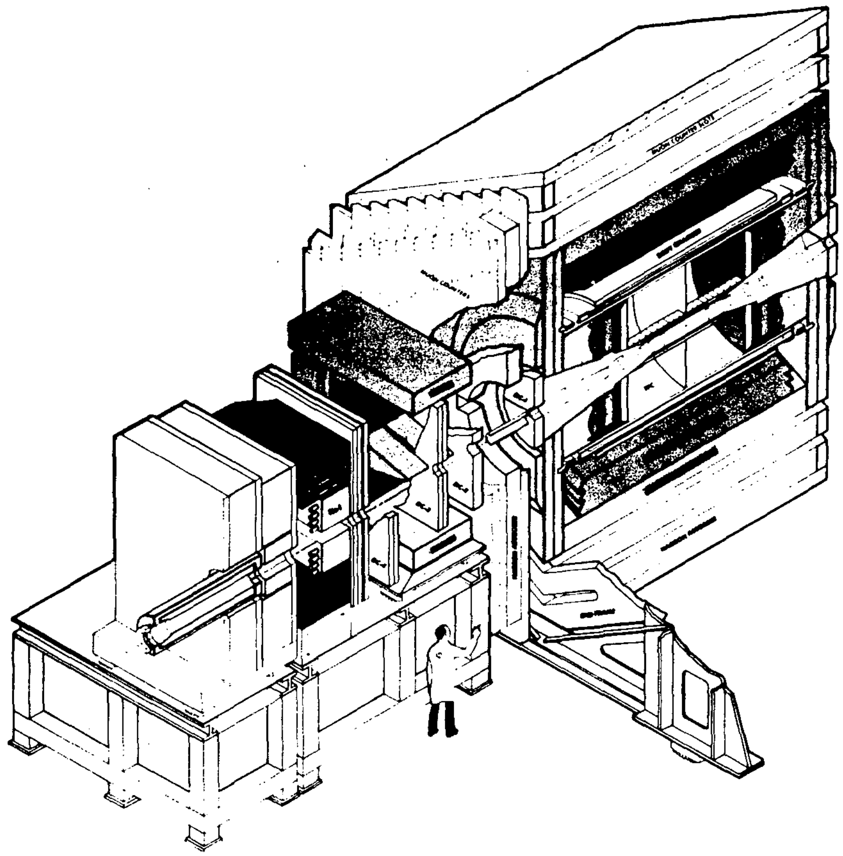

Figure 2.1: The PEP4/9 Detector, showing the central detector and one of the forward detectors

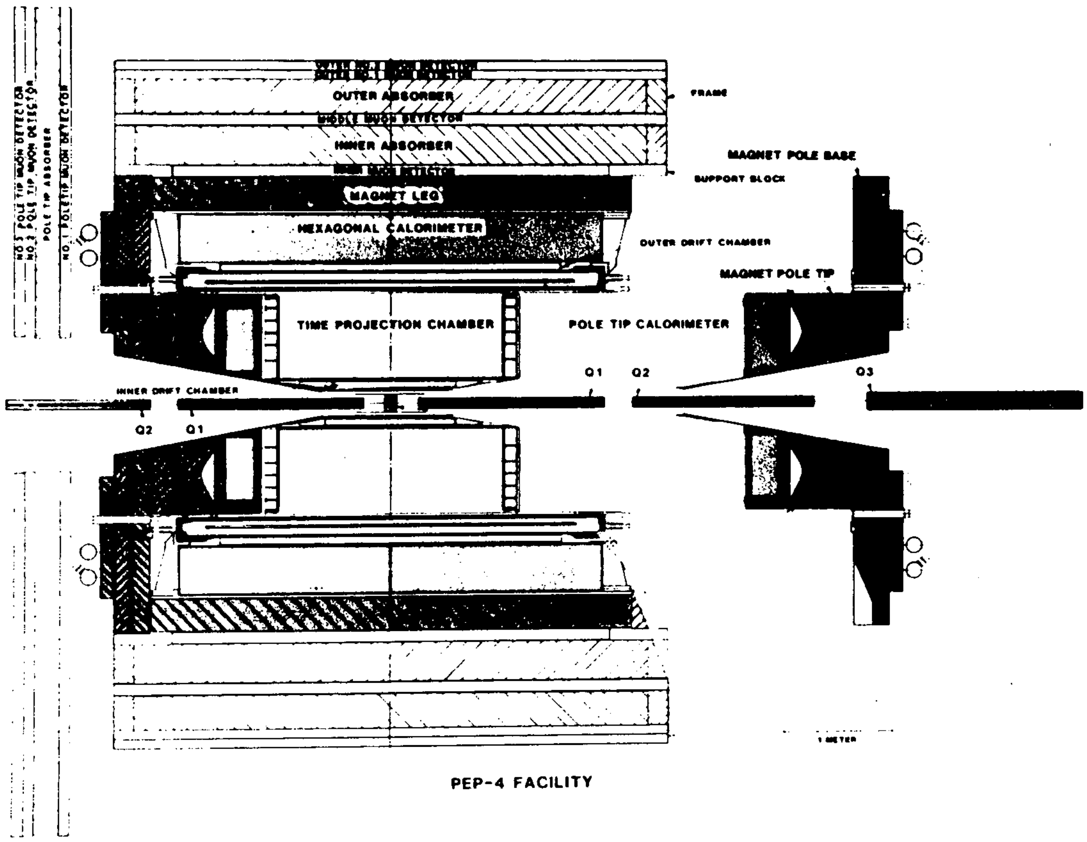

Figure 2.2: Longitudinal section of the central detector, with one pole-tip rolled out

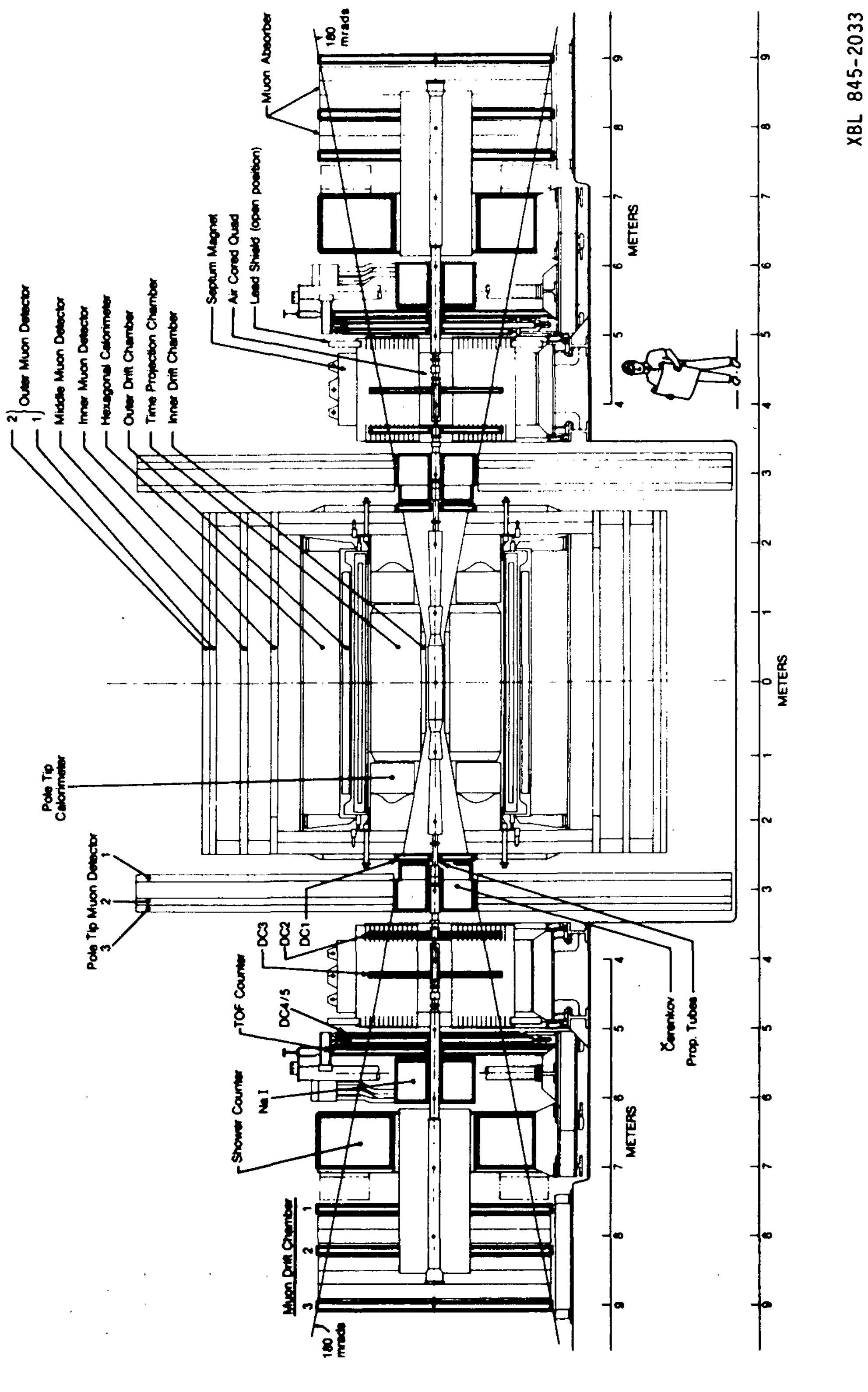

Figure 2.3: Longitudinal section of the detector system, with emphasis on the forward detectors

Table 2.1: Specifications of the central detector

MAGNET	1982-83: 4 kG Al coil solenoid (1.32 X_0 coil package) 1984: 13.2 kG superconducting coil (0.86 X_0 package) Diameter = 2.15 m, length = 3.0 m
TRACKING	Time Projection chamber (TPC): 2.0 m long (in z) at 20 to 100 cm radius (r) Argon-methane (80%-20%) at 8.5 atm. Max. drift 1.0 m in 30 μsec, 50 kV/m drift electric field The azimuth is divided into six 60° sectors. Per sector: 183 proportional wire hits on tracks with $\lvert\cos\theta\rvert < 0.71$, each wire gives r, z and amplitude for dE/dx 15 3-dim space points from induced cathode signals on several of 13,824 channels to give r, ϕ, and z. $\geq$2 3-d points and $\geq$15 wire hits over 97% of 4π sterad Track pair resolution of 1-2 cm dE/dx $\pm$3.0% for Bhabhas, $\pm$3.5% for tracks in jet events $\sigma_p/p < \pm.5\%$ at high momentum position resolution in bending plane is 150 μm, 300 μm in z. Inner drift chamber at 13 to 19 cm radius 8.5 atm Ar-CH_4 (80%–20%) 1.2 m long covering 95% of 4π, with 4 axial layers. Outer drift chamber at 1.19 to 1.24 m radius 1 atm Ar-CH_4 (80%–20%) 3 m long covering 77% of 4π, with 3 axial layers.
POLE-TIP CALORIMETER	Gas, proportional mode, sampling Pb-laminate calorimeter 2 modules, 13.5 X_0 deep, at z = 1.1 m, covering 18% of 4π Argon-methane (80%-20%) at 8.5 atm; total of 51 samples Three 60^0 stereo views, each with 13 and 4 samples in depth Projective strip geometry with 8 mrad angular segment $\sigma_E/E = 11\%/\sqrt{E}$, below 10 GeV, 6% at 14.5 GeV
HEXAGONAL CALORIMETER	Gas, Geiger mode, sampling Pb-laminate calorimeter 6 modules, 10 X_0 deep, 4.2 m long, at 1.2 m radius Argon-methylal(5.5%)-N_2O(2.2%) at 1 atm. Solid angle coverage of 75% (90% including PTC) 3 correlated 60^0 stereo views, using wire and cathode signals in 40 samples (27 and 13 samples in depth) Projective strip geometry with 9 mrad angular segment. $\sigma_E/E = 16\%/\sqrt{E}$, below 10 GeV, 14% at 14.5 GeV

Table 2.2: Specifications of the forward detectors

MAGNETS	2 septum magnets: 1 m long, aperture 2.24 m by 2.1 m $B_{max} = 1.7$ kG; $\int B\,dl \approx 2.6$ kGm; B = 0 on beam axis Each magnet compensated by air core skew quads immediately around the beam pipe.
TRACKING	5 drift chamber (DC) modules at each end DC-1: 4 planes, 2 horizontal, 2 vertical $\pm 10°$, Ar-Ethane (50%-50%) DC-3: 2 vertical $\pm 10°$, Ar-CO_2 (83%-17%) DC-2,4,5: 3 planes, 1 horizontal, 2 vertical $\pm 10°$, Ar-CO_2 (83%-17%) $\sigma_{\mathrm{position}} \approx 300\,\mu$m $\sigma_p/p = \pm\sqrt{(0.008\,p)^2 + (0.025)^2}$ Angular acceptance of system: 22 mrad to 180 mrad
NaI CALORIMETER	Angular acceptance: 22 mrad to 100 mrad at either end Each detector contains 60 individual NaI crystals, 22 inches long with a hexagonal cross section 6 inch apex to apex $\sigma_E/E = \pm 1\%$ at 14.5 GeV Spatial resolution: $\sigma \approx 0.4$ cm
Pb-LAMINATE CALORIMETER	Angular acceptance: 100 mrad to 180 mrad at either end Alternate layers of Pb sheets and plastic scintillator strips set in three 60° stereo views; wave bar readout 54 total layers, 18 X_0 $\sigma_E/E = \pm 15\%/\sqrt{E}$ spatial resolution: $\sigma \approx 1$ cm
TOF	Two planes of scintillation hodoscope at each end; one has 50 horizontal scintillator strips, the other 62 vertical strips Time resolution: $\sigma_T = 0.3$ ns
CERENKOV	1 atm CO_2 radiator, 70 cm long, divided into 12 azimuthal segments at each end Efficiency for electrons > 90% over-all, > 95% over 80% of angular coverage (22 mrad to 180 mrad)

they have a cylindrical geometry centered on the beam line. Moving outwards from the beam line, the elements of the central detector are: an inner pressure wall, the inner drift chamber (IDC), the time projection chamber (TPC), the outer pressure wall, the superconducting magnet package, the outer drift chamber (ODC), the hexagonal calorimeter (HEX), and three layers of muon chambers interspersed with iron. Closing the ends of the cylinder are the two modules of the poletip calorimeter (PTC) and more muon chambers. The following sections contain more detailed descriptions of the detector elements which are relevant to this analysis.

2.2.1 Time Projection Chamber

The Time Projection Chamber does the bulk of the charged particle tracking and is essentially the heart of the PEP4/9 detector. Physically, the TPC is a cylinder 2 meters long and 1 meter in radius. A tungsten wire mesh midplane divides the TPC into two smaller cylinders, each 1 meter long. The midplane is held at a potential of -50 kV relative to the ends of the TPC, creating an axial electric field pointing from the ends towards the midplane. To ensure uniformity of the field, the walls of the cylinder are lined with a grid of conducting rings connected by a chain of precision resistors, the resulting grids being known as field cages. The two endcaps of the TPC contain a total of 12 multiwire proportional chambers, or sectors, to be discussed in more detail below. The TPC volume is filled with a gas which is a mixture of 80% argon and 20% methane at 8.5 atmospheres. The solenoidal superconducting magnet provides an axial magnetic field of 1.325 Tesla in the TPC.

When a charged track passes through the gas filled volume of the TPC, it leaves a trail of ionization along its path. Due to the strong electric field, the ionization electrons drift through the gas at a constant velocity of about 3 cm/μs

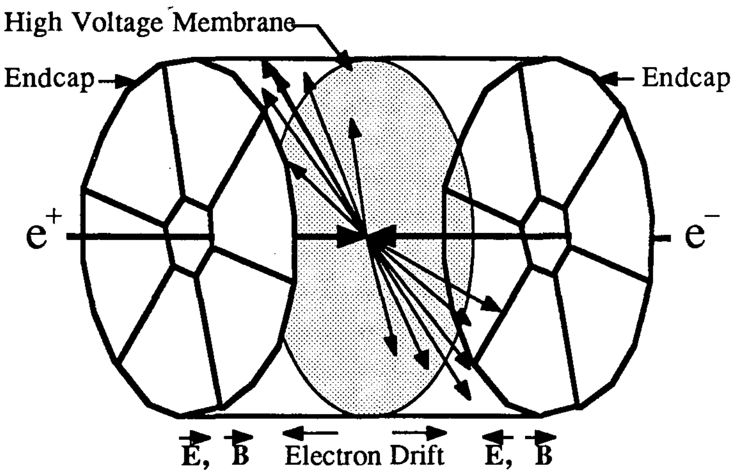

Figure 2.4: TPC, showing electric and magnetic fields

to the endcaps of the TPC, Figure 2.4, where they are detected by the sectors. The sense wires and cathode pads on the sectors provide the coordinates of a track's path in the plane transverse to the beam line, while the coordinate along the beam direction is derived from knowing the time delay between the beam crossing and the arrival of ionization at the sector, together with the electron drift velocity. It is this use of time delay to reconstruct one of the coordinates which gives the TPC its name. Up to 15 three dimensional space points can be reconstructed along each track. In addition, since the sense wires of the sectors operate in proportional mode, the ionization density along a track is reflected in the amplitude of the signal seen at the sense wires. Thus, up to 183 measurements of a charged particle's ionization energy loss (dE/dx) can be obtained, allowing the identification of different particle species, as discussed in Section 3.1.4 .

Figure 2.5 shows a schematic representation of a sector. Each sector has

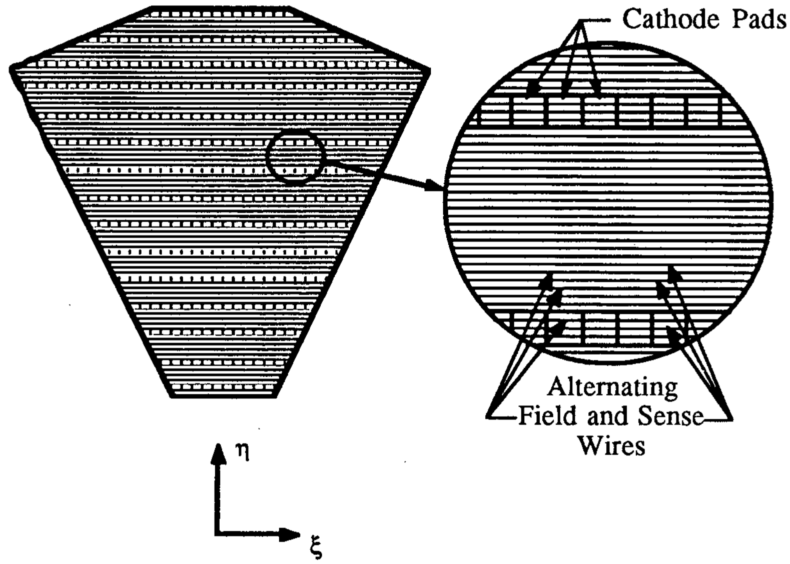

Figure 2.5: A TPC sector

183 sense wires spaced at 4 mm intervals, the wire plane being 4 mm above the sector surface. These wires are held at at a potential of 3400 V, so that when ionization electrons approach a sense wire they are accelerated towards it and induce an avalanche onto the wire. Interspersed between the sense wires are field shaping wires which also help to reduce crosstalk between neighboring sense wires. Another grid of wires 4 mm above the sense wires is held at ground to separate the drift region of the TPC from the avalanche region surrounding the sense wires. A final grid, 16 mm above the sector surface is used as an electric shutter, so as to only allow ionization to drift into the avalanche region if there has been a prepretrigger (Section 2.2.5). The purpose of this gated grid is to reduce the flux of positive ions, liberated in avalanches on the sense wires, which diffuse back into the drift region of the TPC. These ions create a problem as they produce distortions of the electric field, complicating track reconstruction.

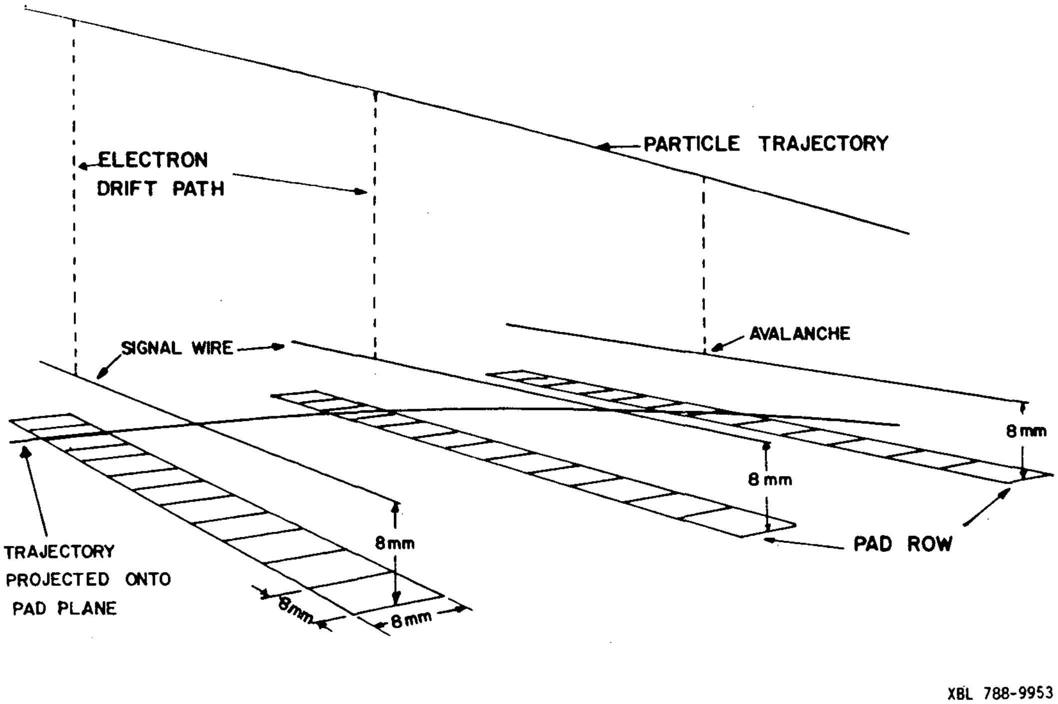

Figure 2.6: Track detection in the TPC

Underneath fifteen of the sense wires in each sector, the cathode plane is segmented into 7.5 mm square pads. Due to the capacitive coupling between the pads and sense wires, an avalanche occurring on a sense wire will also induce a signal on typically 2-3 of the pads below. Thus, in the local sector coordinates of Figure 2.5, both wires and pads provide the ξ coordinates along a charged particle's path, while the pads also provide the η coordinates. Figure 2.6 is a simplified representation of the detection process in the TPC.

2.2.2 Drift Chambers

The primary function of the drift chambers is to provide fast signals for use in the trigger decision. In addition, the ODC is used to help determine whether

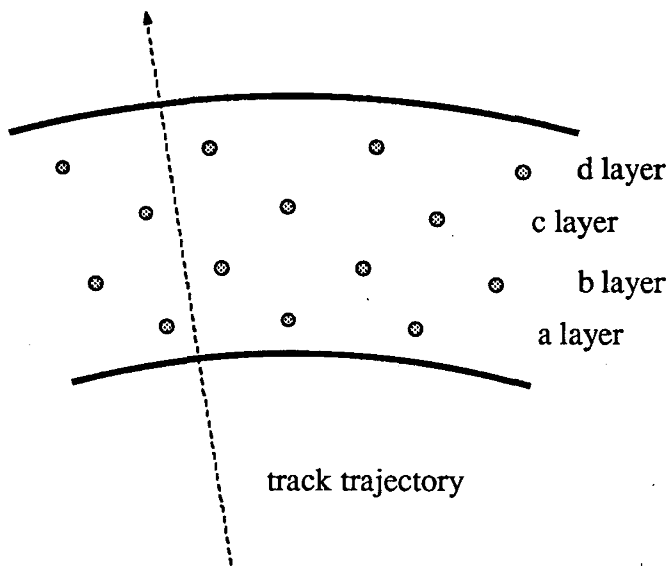

Figure 2.7: A cross section of the IDC

a photon has converted in the magnet package before entering the HEX. The inner drift chamber consists of four concentric layers (denoted the a, b, c, and d layers) of 60 sense wires each, with alternate layers rotated by 3^0 in azimuth, so that the drift cells are staggered. A cross section of the IDC is depicted in Figure 2.7. The IDC is within the TPC pressure volume and therefore operates in 8.5 atmospheres of argon-methane gas. The ODC, mounted on the outside of the superconducting coil cryostat, has three layers (known as the e, f, and g layers), each with 216 sense wires. The ODC operates in the argon-methane gas from the TPC, but at a pressure of 1 atmosphere since it is outside the pressure volume. The ODC and IDC are discussed further as trigger elements in Section 2.2.5 .

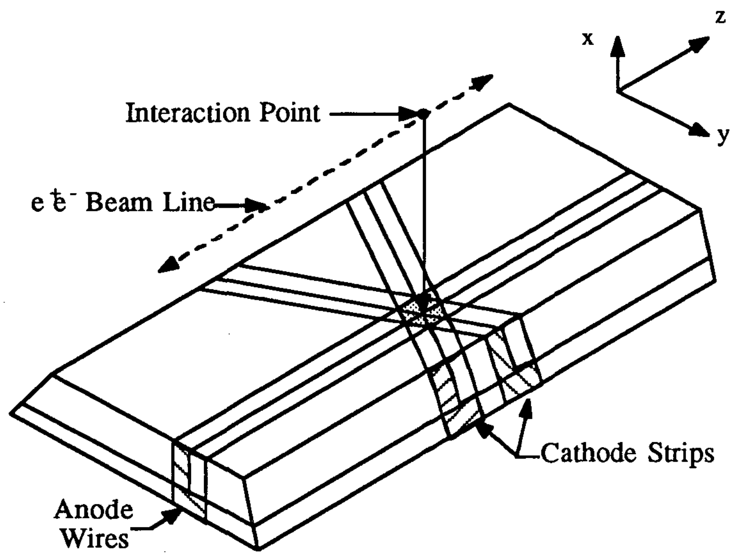

Figure 2.8: A HEX module

2.2.3 Hexagonal Calorimeter

The hexagonal calorimeter [11,12] serves to detect photons which, having no electric charge, are not seen in the TPC. The HEX is divided into six modules, each module covering 60^0 in azimuth. The modules are roughly 4 meters long, and have a trapezoidal cross section, as shown in Figure 2.8. Local coordinates x, y, and z are defined for each module, with the origin taken as the interaction point.

Each HEX module consists of a stack of 40 layers of 3.2 mm thick lead laminate (corresponding to a total depth of 10 radiation lengths), alternating with gaps filled with a gas mixture of Argon-methylal-N_2O. Strung axially in the gaps at 5 mm intervals are anode wires held at a potential of 1400 volts. Nylon filaments (which serve to stop Geiger discharges along the anode wires) are strung perpendicular to the wires every 10 mm. The surface of the laminate on either side of the gap consists of aluminum cathode strips. The strips immediately above and below an anode wire are oriented at $+60^0$ and -60^0 with respect to the wire.

When a photon enters the HEX, the lead generally initiates its conversion to an electron positron pair. The electron and positron will then emit bremsstrahlung photons which will again convert, leading to the development of a shower of electrons and positrons in the calorimeter. The size of this shower will be related to the energy of the initial photon.

Electrons or positrons passing near an anode wire leave a trail of ionization which will initiate a Geiger discharge on the wire. This discharge will propagate along the wire until it encounters a region of depleted electric field caused by the nylon filaments. In the Geiger mode the charge collected on the wire will be quite large, and essentially independent of the amount of ionization which initiated the discharge. A signal will also be induced on the cathode strips running above and below the discharge region. Thus signals are available in three stereo views to determine the exact location of the discharge.

The anode wires and cathode strips of the first 27 and last 13 layers are ganged together in depth to form two submodules. Moreover, within the submodules signals are ganged together in a projective geometry, so as to create channels in the HEX which subtend a constant solid angle as viewed from the interaction region, the channels being about 9 mrad wide.

2.2.4 Poletip Calorimeter

The poletip calorimeter [13] is similar to the HEX in that it consists of lead laminates alternating with gas gaps, but the laminates are disk shaped rather than rectangular, furthermore the PTC sense wires are run in the proportional mode as opposed to the Geiger mode. Since the PTC is inside the pressure

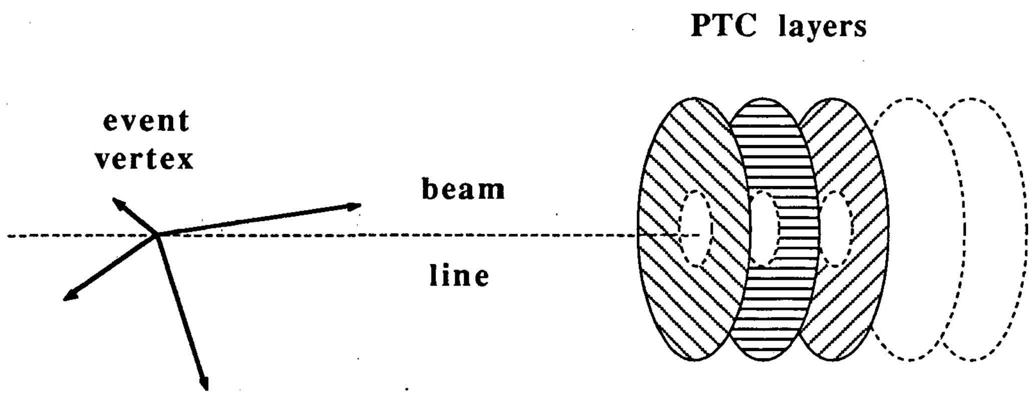

Figure 2.9: Layers in a PTC module

volume of the TPC, the sense wires, which are held at about 2800 V, operate in 8.5 atmospheres of argon-methane. Each PTC module consists of 51 layers, presenting a total depth of 13.7 radiation lengths to incoming photons. Again, each module is divided into two submodules, the front submodules having 39 layers with sense wires at 1 cm spacing, the back submodules having 12 layers with 2 cm wire spacing.

In contrast to the HEX, each gas gap contains only sense wires, with no corresponding cathode strips. The wires are strung along three different axes, with the wires in adjacent gaps oriented at 60^0 intervals, Figure 2.9. Thus, showers which penetrate 3 or more layers can be reconstructed in three stereo views, known as the P, Q, and R views. The wire spacing in each submodule increases gradually with distance from the interaction point to achieve, as in the HEX, a projective geometry.

2.2.5 Trigger System

Although there are 408,000 beam crossings per second in the PEP ring, interactions of interest occur at a far smaller frequency, at a level of around 1 Hz. The time required to read out the thousands of signals from the detector is around 20 milliseconds, which precludes reading out the detector at each beam crossing. Therefore, for each beam crossing a relatively fast decision must be taken as to whether a potentially interesting interaction has occurred. This decision is made by a collection of circuits which process selected signals from the detector, the whole system being known as the trigger. For obvious reasons, an efficient and reliable trigger is crucial to the performance of the detector system.

The decision as to whether or not to read out the detector is actually made in three separate stages, known as the pre-pretrigger, pretrigger, and trigger decisions. These decisions represent three progressive levels of sophistication in the electronics, each decision requiring the previous. Thus, the pretrigger is enabled by the pre-pretrigger, and the trigger is enabled by the pretrigger. The pre-pretrigger and pretrigger decisions are very fast, using detector elements which provide prompt signals and requiring that these signals reflect an interesting event only in a rather loose sense. If the pretrigger is not satisfied, the electronics are reset before the next beam crossing. On the other hand, if the pretrigger is satisfied the ionization in the TPC is allowed to drift to the sectors. Then, using the more detailed information available at this time, the trigger logic places more stringent requirements on the signals from the detector. If these requirements are met, the detector signals are read out into a large buffer which is accessed by an online computer for further analysis and transfer to tape. Otherwise, the electronics are reset in preparation for the next beam crossing.

The trigger system uses signals from both charged particles and neutrals in the overall trigger decision. For the current analysis, however, the elements of the trigger which use signals from the charged tracks are most relevant. Therefore, a brief discussion of the charged particle trigger is presented below, while a more detailed discussion may be found in [14] or [15]. The neutral elements of the trigger are described in [12] and [13].

The pretrigger in the charged particle branch of the trigger uses signals from three sources: the IDC, ODC, and signals from tracks which pass through the TPC endcaps, prompting immediate avalanches onto the sector sense wires. These latter signals are known as TPCF (for TPC Fast) signals. The IDC, ODC, and TPCF elements of the pretrigger are discussed below.

The IDC pretrigger element requires the detection of a track traveling in a radial direction, within a tight time window around beam crossover. Denoting the time necessary for a track's ionization to drift to a wire in layer i by t_i, the relation $t_a + t_b \simeq constant = 180\ ns$ (or, equivalently, the same relation for t_c and t_d) will hold for tracks traveling in a radial direction. This relation, which is a consequence of the azimuthal staggering of drift cells in alternate layers, will not hold for tracks which cross the cell in a non radial direction. Therefore, signals from the IDC are required to satisfy the condition that the total drift time for hits in adjacent layers be $180\ ns \pm 30\ ns$. Signals which pass this requirement are logically OR'ed into 12 overall IDC pretrigger signals, each covering 30^0 in azimuth.

The ODC pretrigger element is built from basic units known as ODC pretrigger cells. An ODC pretrigger cell (Figure 2.10) consists of 3 drift cells from the e layer, the 4 drift cells from the f layer which border on the 3 e layer cells, and the 5 g layer cells which border on the 4 f layer cells. Adjacent ODC pretrigger cells therefore overlap, as they share 1 f layer cell and 2 g layer cells. An ODC pretrigger cell signal is generated if at least 2 wires from different layers within the cell fire within 300 ns (corresponding to the maximum drift time) of

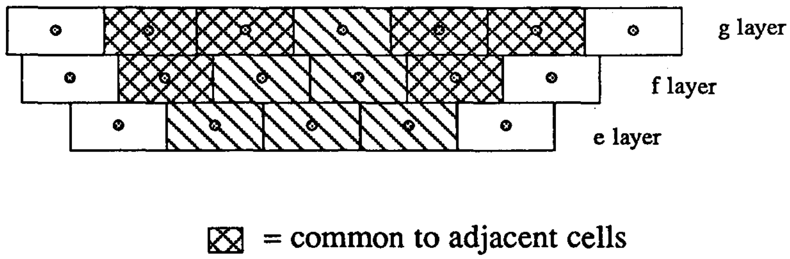

Figure 2.10: An ODC pretrigger cell

the beam crossing. As in the case of the IDC, these signals are OR'ed together to form 12 azimuthal wedges, each covering 30^0.

Signals from the sense wires on the sectors follow two paths, one leading to (after shaping and digitizing) the online computer, the other to the trigger system. In the trigger, signals from adjacent wires are considered together in groups of 8, known as majority units. A majority signal is generated for a given majority unit if a minimum number of wires (usually 4) have signals above a preset threshold. Furthermore, adjoining sectors are joined together in groups of two (known as supersectors), so that, for instance, supersector 0 is an OR of sectors 0 and 1. The 30 μs drift time of the TPC is divided into 64 time buckets, so that the majority units divide the TPC volume into cells which are roughly 8 wires in radius, 120^0 (or two sectors) in azimuth, and .15 μs in drift time. A TPCF signal is generated by a majority signal which occurs within 2

μs of beam crossing. However, because of noise near the beam line, only those majority signals due to tracks making an angle of greater than 30^0 with respect to the beam direction are enabled to produce a TPCF signal.

The charged particle pretrigger decision is made by examining the IDC, ODC, and TPCF pretrigger signals which have been generated. Only certain combinations of these signals will satisfy the final pretrigger requirement. Functionally, this is accomplished by bringing the IDC, ODC, and TPCF signals in on the address lines of RAM's (Random Access Memory units). Each address in a RAM then corresponds to a certain combination of pretrigger signals. The RAM's are pre-loaded by a computer so that addresses corresponding to valid combinations of pretrigger signals contain a 1, while other addresses contain a 0 . The output line of the RAM then reflects the pretrigger decision. The pretrigger generally is set to look for IDC signals correlated in azimuth with ODC signals or IDC signals correlated with TPCF signals. For the data used in this analysis, the charged particle pretrigger required either 2 separate IDC-ODC coincidences, 2 separate IDC-TPCF coincidences, or 1 IDC-ODC coincidence together with 1 IDC-TPCF coincidence.

The pre-pretrigger uses essentially the same elements as the pretrigger, in a somewhat looser combination. The pre-pretrigger logic was necessitated by the addition of the gated grid, since the requirement of 4/8 wires in the majority units is difficult to satisfy with the grid closed. The function of the pre-pretrigger is to open the grid, allowing ionization to drift in to the sectors to form the TPCF signals.

The pre-pretrigger decision is formed in the same manner as the pretrigger, except that instead of TPCF signals, the pre-pretrigger uses TPCE signals, which are analogous to TPCF signals except that only 1/8 wires are required instead of 4/8. The pre-pretrigger then requires 2 IDC signals (separated by at least 90^0

in azimuth) in conjunction with either an ODC signal or 2 TPCE signals from different sectors. The pre-pretrigger is also satisfied if a total energy sum signal from the calorimeters exceeds a rather low threshold.

If the pretrigger requirements have been satisfied, the ionization in the TPC is allowed to drift to the sectors and the resulting signals are examined by the trigger logic. The charged particle trigger has several branches, but the most sophisticated (and most important for this analysis) is known as the ripple trigger. The ripple trigger essentially examines the majority signals previously mentioned for evidence of tracks which point back towards the interaction point. 'Ripple tracks' are started at the outermost edges of the TPC and then propagated, or 'rippled', to the inner radius. A ripple track can be initiated either by a majority signal which satisfies the TPCF requirement or a majority signal from the two wire groups highest in radius, with no time restriction. Once started, the ripple track is propagated by logic circuits which look for majority signals inwards in radius and later in drift time. If there are majority signals which propagate the ripple track all the way to the inner radius, the arrival time of the ripple track at the inner radius is examined to see if it is in coincidence with a time window expected for a track originating from the interaction point. If so, the ripple track is further required to be azimuthally correlated with either a TPCF or ODC pretrigger signal. Ripple tracks which pass all these requirements are then input to a pre-loaded RAM, as in the case of the pretrigger signals, to select desired combinations. For this analysis, two distinct ripple tracks were required in order to satisfy the trigger.

Chapter 3

Data Analysis

The data on which this analysis is based were obtained during the 1984-1985 and 1985-1986 running cycles. Roughly 1000 tapes of raw data were collected, corresponding to an integrated e^+e^- luminosity of 64 pb^{-1}. This chapter describes the process of reducing these 1000 tapes to the final set of events used to determine the cross section for $\gamma\gamma \rightarrow \rho^0\omega$.

Raw data from the PEP-4 detector is refined by a large set of programs known collectively as the offline analysis. This refinement is accomplished in several stages, each corresponding to a pass through the data. In the first stage, the trigger information is examined in detail and a more considered trigger decision is made. Next, a rudimentary pattern recognition is done to find the tracks in the TPC. The third pass serves to monitor and refine time dependent parameters which are needed for subsequent analysis. In the fourth pass, the detailed track reconstruction, dE/dx analysis, and vertex fits are done. The final pass undertakes the reconstruction of photons from hits in the calorimeters, together with a classification and selection of events.

The preceding analysis yields a refined set of events for physics analysis. In searching for a given final state however, further selection is necessary. In Section 3.2 the process of selecting the $\pi^+\pi^-\pi^+\pi^-\pi^0$ final state is described in detail.

3.1 Offline Analysis

The offline analysis has two primary goals: first, to select and retain only those events of interest for subsequent physics analysis, and second, to extract from the raw data the 4-vectors of produced particles at the event vertex. The following subsections chronicle only the major steps in this process, but further details may be found in [14] and [17].

3.1.1 Pass 1- Preanalysis

Though originally the preanalysis program was run offline, it now is run as part of the data collection process. The function of preanalysis is to reject events (primarily from cosmic rays or beam gas scattering) which are not of interest before they are written to tape. The fraction of events rejected at this stage is approximately 40%, resulting in considerable savings in both tapes and CPU time. In a scan of rejected events, it was found that preanalysis rejects a legitimate event once in approximately 6,000 triggers. Moreover, the few legitimate events which were rejected were events which had only two tracks, and had a special topology which made pattern recognition difficult.

The preanalysis decision is based on a more careful analysis of the raw data than is possible in the trigger hardware. The distance of closest approach to the interaction point is obtained for each track by using the TPC majority units in conjunction with the signals from selected pad rows. The cuts which are subsequently applied vary with the polar angle of the track but tracks are typically required to extrapolate to within 14 cm of the interaction point in the z direction and to within 10 cm in the x-y plane. For events with a neutral or charged-neutral trigger, the calorimeter information is examined to ensure that the energy deposition is consistent with that expected from a particle originating at the interaction point.

3.1.2 Pass 2- Pattern Recognition

The task of track reconstruction is initiated in Pass 2. At this stage the 3-dimensional information in the pad signals is used as input to the TPC pattern recognition algorithm, which identifies and assigns preliminary orbits to the tracks in the event. The pattern recognition algorithm finds tracks regardless of whether they originate from the interaction point, and, for tracks which cross three or more pad rows, is estimated to be at least 95% efficient.

This pass also serves to further filter the events. The use of TPC reconstructed orbits together with calorimeter information allows the imposition of even tighter cuts to discriminate against background. Pass 2 rejects approximately 30% of the events it encounters.

3.1.3 Pass 3- Monitoring of Constants

There are a number of calibration parameters used in the analysis which vary in time. Examples of these parameters include the electron drift velocity in the TPC, the TPC gas composition, gain on the wires, etc. The best way to track the time variation of many of these parameters is by examining distributions of signals from the detector. The third pass through the data is therefore dedicated to extracting more accurate values of the time dependent calibration parameters, which are then written into a database for use in subsequent analysis.

3.1.4 Pass 4- Track Reconstruction

The fourth pass through the data finishes the bulk of the analysis. First, the space points associated with tracks in Pass 2 are refined, taking into account electrostatic distortions in the TPC and using the z information from wire hits. Position errors are assigned to the improved space points and they are fit to a helix. Then, tracks which pass near the interaction point are constrained to have a common origin in a vertex fit. This fit, by using an additional space point, considerably improves the momentum accuracy and yields the final vertex momenta assigned to particles in the event.

A unique feature of the TPC is the ability to do particle identification via the measurement of ionization energy loss. The method relies on the fact that the most probable value of the energy loss for a charged particle traveling through a sample of gas is a function of the particle's speed. Thus, a simultaneous measurement of energy loss and momentum allows the determination of a particle's mass.

A charged particle passing through a gas loses energy through collisions with electrons. The majority of these collisions correspond to small energy transfer interactions with electrons at large distances, but occasionally the particle will have a large energy transfer interaction with an electron in a close collision. If one makes many measurements of a particle's energy loss per unit distance in a gas, the resulting distribution (known as a Landau distribution) will have a long tail due to large energy transfer collisions. For relativistic particles it is the number of low energy transfer collisions which is most sensitive to the particle's speed. Therefore, for the measurement of dE/dx, the analysis code discards the Landau tail and uses the mean of the lowest 65% of the measurements. The dE/dx value thus obtained has a resolution which depends on the number of measurements, Figure 3.1.

The particle identification algorithm assigns to each track a χ^2 for the hypothesis that the track is an electron, muon, pion, kaon, or proton. This is done by measuring the distance (in standard deviations) from the point $(p, dE/dx)_{measured}$ to the theoretical dE/dx vs. p curve for each particle hypothesis. As can be seen from Figure 3.2, a plot of observed dE/dx vs. momentum, the TPC can (except for crossover regions) separate particle species over a wide momentum range.

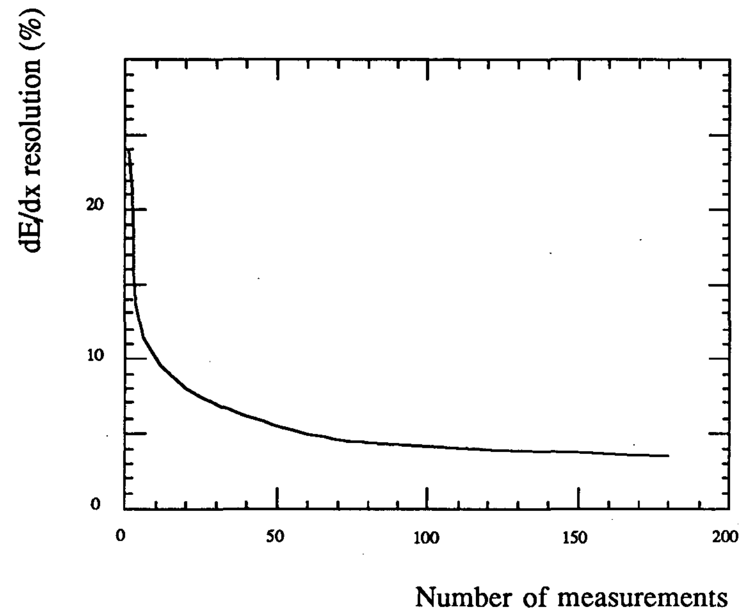

Figure 3.1: dE/dx resolution as a function of the number of measurements

3.1.5 Pass 5- Photon Reconstruction and Event Classification

In the first stage of Pass 5, an attempt is made to classify events into various physics or background processes, such as one photon annihilation, Bhabha's, cosmic rays, etc. This classification is carried out by the SELTWOGAM [18] program. SELTWOGAM divides events into a number of categories based on total energy, number of tracks, event topology, etc. It then rejects categories deemed uninteresting, mainly Bhabha's, cosmic rays, and beam gas events.

Pass 5 also serves to process the calorimeter information. The HEX analysis first uses the three stereo views provided by the wire and cathode strip signals to reconstruct the position of hits, or 'clusters' in the modules. Then, the number of Geiger cells which fired in each cluster is determined and translated into an energy. Based on ODC information, a judgement is made as to whether the

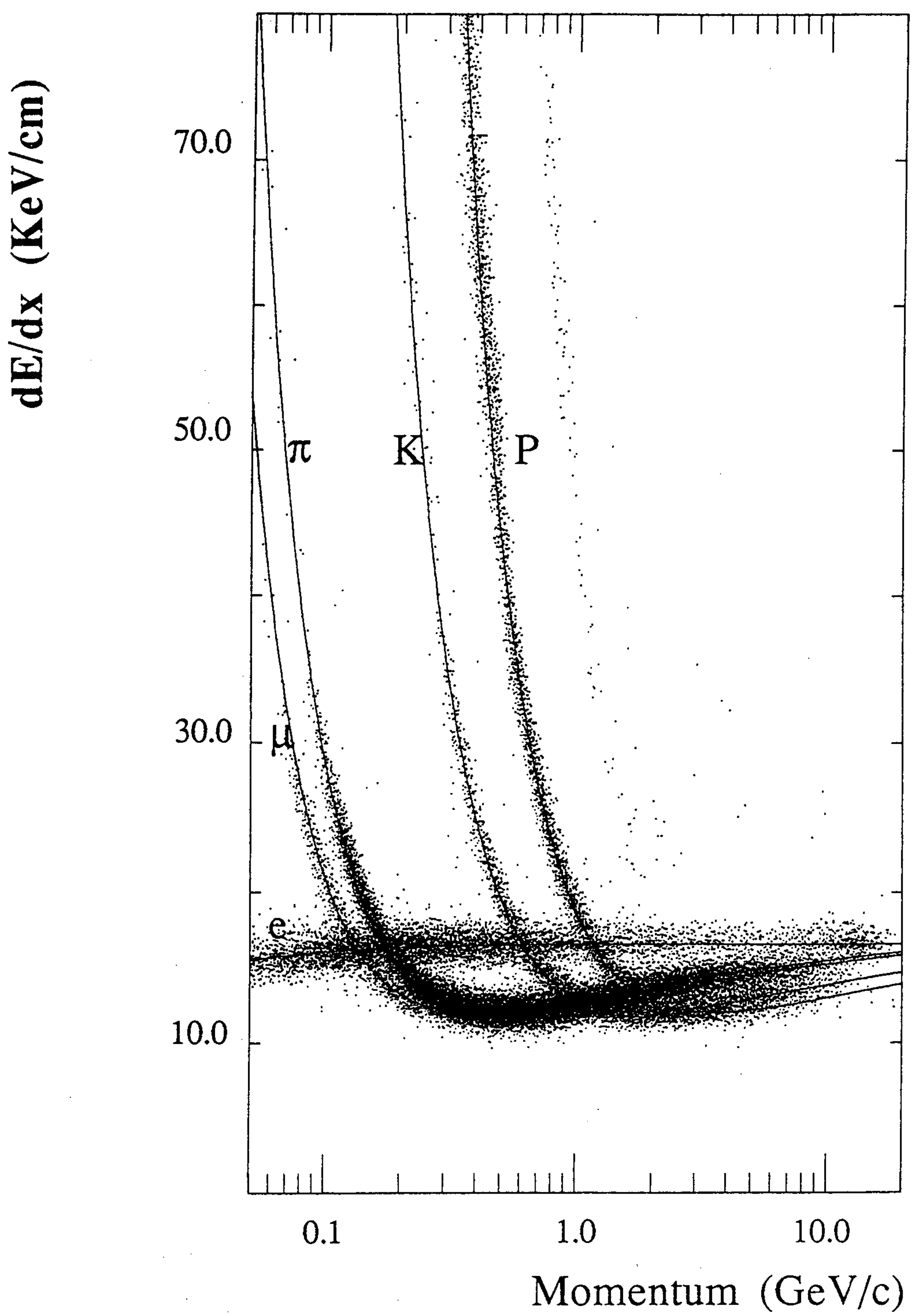

Figure 3.2: dE/dx vs momentum for tracks with at least 80 dE/dx measurements

cluster is due to a photon which converted in the coil. If there was a conversion, the cluster is assigned some additional energy to correct for energy lost by the conversion electrons in the coil. Next, the trajectories of charged tracks are examined to see if they pass near clusters found in the HEX. If the distance of closest approach of a charged track to a cluster is less than 8 cm, the cluster is considered to be track associated and is discarded. Finally, clusters whose angular separation (as seen from the interaction point) is less than 60 milliradians are judged to be due to the same photon and are merged. As mentioned in Section 3.2.2, more restrictive cuts are required for the particular needs of this analysis.

The PTC analysis begins by locating peaks in each of the three wire views, P, Q, and R. It then looks for clusters, requiring coincidence of the peaks in all three views. This has important ramifications for the reconstruction of low energy photons, since it means that a low energy photon must initiate a shower which penetrates at least three layers. Once a cluster has been found it is assigned an energy based on a linear extrapolation of the calorimeter response to 14.5 GeV electrons from Bhabha events. The PTC analysis does not merge clusters or eliminate clusters due to charged tracks.

3.2 $\pi^+\pi^-\pi^+\pi^-\pi^0$ Event Selection

The process $\gamma\gamma \rightarrow \rho^0\omega$ is expected to have a small cross section, hence a careful separation of true $\rho^0\omega$ events from events due to other processes is essential. Final states of higher multiplicity may resemble a $\rho^0\omega$ final state if particles are not reconstructed; the characteristic of low momentum particles boosted in the z direction typical of two photon events makes this a likely occurrence. Final states of lower multiplicity may also contribute to the background through production of particles in secondary interactions or 'fake' photons in the calorimeters. Because low energy charged pions can interact in the coil and produce hits in the calorimeters which are interpreted as photons, the copiously produced $\pi^+\pi^-\pi^+\pi^-$ final state must be carefully excluded.

The first step in the event selection has already been described, namely, the rejection of beam gas and cosmic ray events in the offline analysis. In the second step of the selection, requirements are placed on the charged tracks consistent with the expectation of four charged pions originating from a common vertex. The third step requires the presence of photons in the calorimeters consistent with the production of a π^0 in the event. Finally, knowledge of the kinematics of photon-photon collisions is exploited in a constrained fitting procedure. This fit simultaneously tests the hypothesis that the event is an exclusive $\pi^+\pi^-\pi^+\pi^-\pi^0$ final state, and, for exclusive events, improves on the measured momenta.

3.2.1 Charged Particle Selection

The first criterion imposed on the charged tracks in the event is that there be exactly four tracks, and that the four tracks balance charge. While this requirement will result in the loss of some true $\pi^+\pi^-\pi^+\pi^-\pi^0$ events, it is necessary in order to reduce the background from final states of higher multiplicity. The detector simulation should correct for the loss of $\pi^+\pi^-\pi^+\pi^-\pi^0$ events due to this cut, with the exception of events in which a pion backscatters outside the TPC (discussed in Section 5.1.4).

Next, requirements are placed on each of the charged tracks :

- No track may be part of a conversion pair identified by the pairfinder program. Due to the rather low (and poorly known) efficiency for finding conversion pairs, events in which a photon conversion is detected are discarded.

- Each track is required to extrapolate back to the event vertex within 8 cm

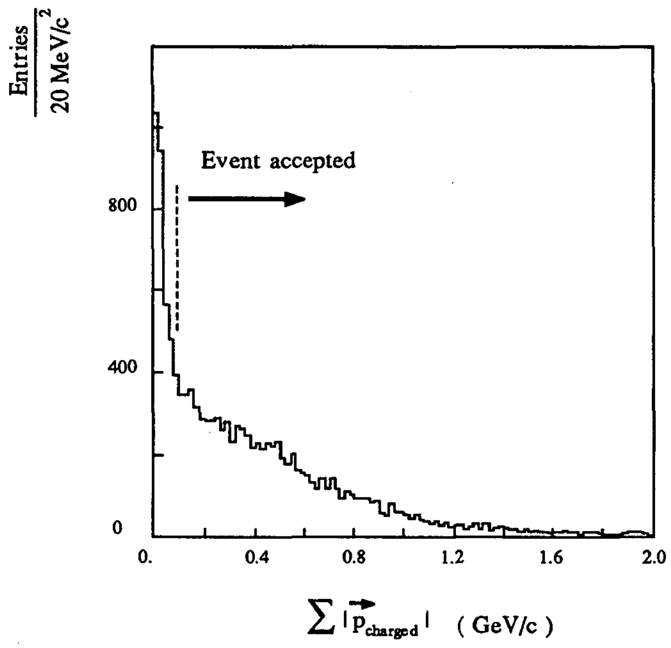

Figure 3.3: The distribution of $|\sum \vec{p}_{charged}|_{\perp}$

in the z direction and within 3 cm in the x-y plane. This is a rather loose cut, but a more stringent requirement is made during the kinematic fitting, Section 3.2.3

- No track may be unambiguously identified as something other than a pion. Specifically, if $\chi^2_{pion} > 16$, then $\chi^2_{electron}$, χ^2_{muon} , χ^2_{kaon} , and χ^2_{proton} must all be greater than 4 for the track to be accepted.

Finally, in order to reject the $\pi^+\pi^-\pi^+\pi^-$ final state, the vector sum of the momenta of the four charged particles is required to have component perpendicular to the beam direction (abbreviated as $|\sum \vec{p}_{charged}|_{\perp}$) of at least 80 MeV/c. A distribution of this quantity is shown in Figure 3.3.

3.2.2 Photon Selection

While the PEP-4 detector is well suited for tracking low energy charged particles, the detection of low energy neutrals presents some difficulties. The calorimeters, designed primarily for one photon annihilation physics, are inefficient and have poor energy resolution at low energies. In addition, low momentum charged pions are likely to scatter at large angles in the coil, making the association of hits in the calorimeters with charged tracks more difficult. Finally, a photon which creates a broad shower in a calorimeter may be interpreted by the pattern recognition programs as two or more photons, leading to an error in the number of photons found in the event. Despite these problems, with a careful selection of photons reasonable signals may be extracted from the data.

The first step in the selection of photons involves a more restrictive association of hits in the calorimeters with charged tracks than that already mentioned in Section 3.1.5. Based on the momentum measured in the TPC, each track is extrapolated to see where it should intersect a calorimeter. Then, if a hit is found in the calorimeter near that point, the hit is judged to be track associated and discarded. For the PTC, hits are discarded if the angular separation (as measured from the vertex) between the hit and the extrapolated position of a charged track is less than 8^0, corresponding to a distance of about 16 cm at the face of the PTC. For the HEX, hits are discarded if they are within 24^0 (corresponding to a distance of about 70 cm). This rather severe cut is necessitated by the tendency of low momentum charged pions to interact in the coil and produce hits in the HEX which are quite distant from the extrapolated track position based on TPC information. Figure 3.4 shows the distribution of angular separation between tracks and photons.

Next, the calorimeter hits which have not been rejected on the basis of track association are examined to see if there are other hits nearby. As mentioned

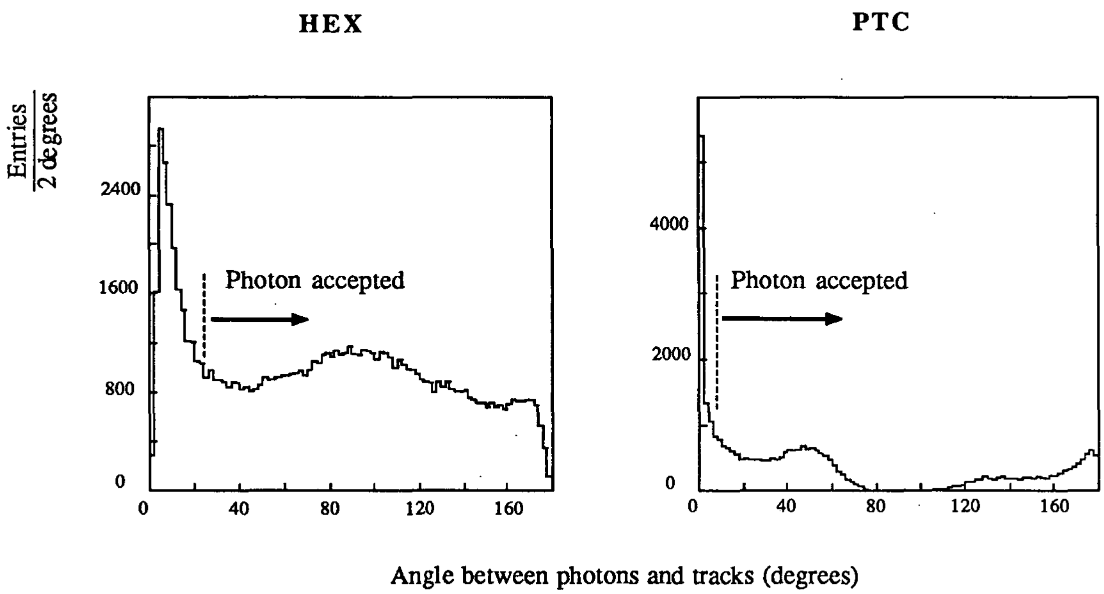

Figure 3.4: Angular separation of tracks and photons

above, the pattern recognition routines sometimes interpret a single photon as two or more hits, so hits are merged based on their angular separation (measured from the vertex) . Any hits separated by less than 15^0 are merged in the HEX, and hits separated by less than 10^0 are merged in the PTC. The distribution of photon separation is shown in Figure 3.5.

At this point, only the events which have exactly two good photons are retained. To ensure that this requirement does not reject many legitimate $\pi^+\pi^-\pi^+\pi^-\pi^0$ events the following analysis was undertaken. First, a sample of exclusive $\rho^0\rho^0$ events was selected and the photons in this sample were examined. The events were selected from the four pion sample by requiring that the transverse component of the vector sum of the charged momenta be less than 20 MeV/c. In addition, selected events were required to satisfy the invariant mass condition 650 MeV/c^2 $< mass(\pi_1^+, \pi_2^-), mass(\pi_3^+, \pi_4^-) <$ 900 MeV/c^2 for at least one per-

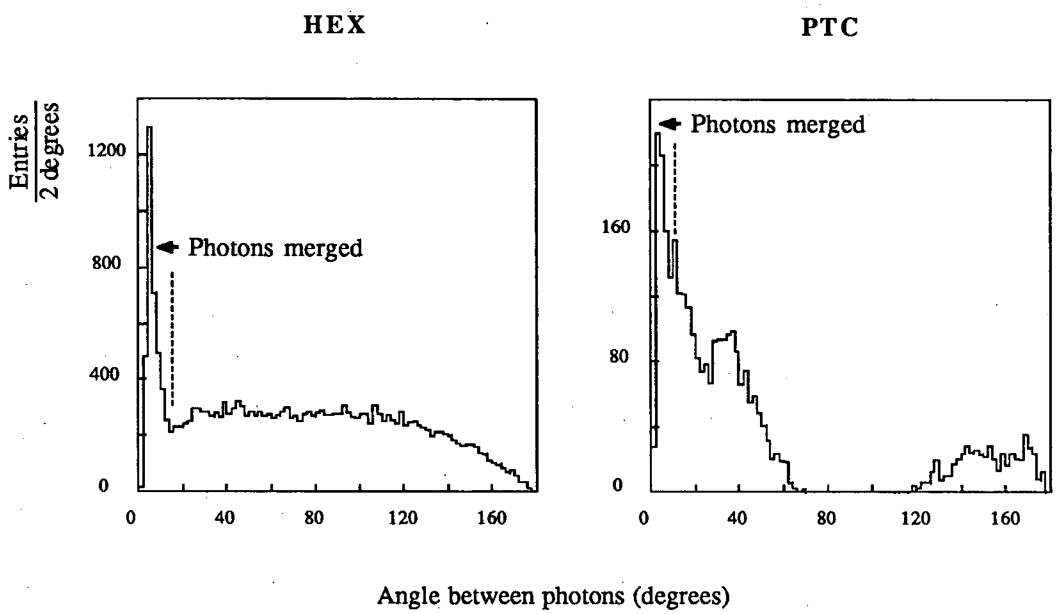

Figure 3.5: Angular separation of photons

mutation of the charged pions. To the extent that these cuts result in a pure $\rho^0\rho^0$ sample, no photons should be found in the events. In fact, 64 out of 318 events were found to have one or more 'good' photons in the event. This would indicate that at most 20% of the $\pi^+\pi^-\pi^+\pi^-\pi^0$ events could be rejected on the basis of requiring no more than 2 photons in the event.

To further study this question, a sample of roughly 100 $\rho^0\rho^0$ and $\pi^+\pi^-\pi^+\pi^-\pi^0$ event candidates were hand scanned. While it is difficult to derive a quantitative estimate of possible losses from such a scan, some qualitative conclusions were drawn:

- The calorimeters are quite 'clean', i.e. random noise rarely, if ever, shows up as a photon.
- The 24^0 track association cut on HEX photons is really necessary to eliminate fakes due to charged pions.

- The number of legitimate $\pi^+\pi^-\pi^+\pi^-\pi^0$ event candidates in the sample of events with 3 'good' photons is down by about a factor of 10 from the number of $\pi^+\pi^-\pi^+\pi^-\pi^0$ candidates in the sample of events with 2 'good' photons.

Another indication that few $\pi^+\pi^-\pi^+\pi^-\pi^0$ events are lost by requiring exactly 2 photons is provided by a comparison of the $\gamma\gamma$ invariant mass distributions for events containing 2 photons and events containing 3 photons (Figures 3.8 and 3.9). Evidence for π^0 production is clear in the events containing 2 photons, while the events containing 3 photons show little or no π^0 signal. A more quantitative approach relying on $|\sum \vec{p}_{charged}|_\perp$ distributions yields a loss estimate of 15%, as discussed in Section 5.1.4 .

Fiducial cuts are imposed on the photons to ensure that they are in a region where the calorimeter response is reasonably well known. HEX photons are used if $| y_{hex} |< 75$ cm and $| z_{hex} |< 180$ cm (y_{hex} and z_{hex} are defined in Section 2.2.3) . Photons in the PTC are required to have a radius between 35 and 80 cm.

Finally, the photon energies (after the constrained fit discussed in the next section) are required to be greater than 50 MeV for HEX photons and greater than 100 MeV for PTC photons, Figure 3.6. The purpose of this cut is twofold; first, to reduce background from fakes, and second, to keep the photons in an energy range where the efficiency of the calorimeter has been measured.

3.2.3 Kinematic Fitting

In Section 1.1.2 it was observed that the $\gamma\gamma$ system is usually produced with a small component of momentum transverse to the beam direction. Therefore, if the final state X produced from the photon photon interaction has been completely reconstructed, the transverse component of the sum of all particle momenta (denoted as $|\sum \vec{p}\,|_\perp$) should be small. For this reason, it is common in

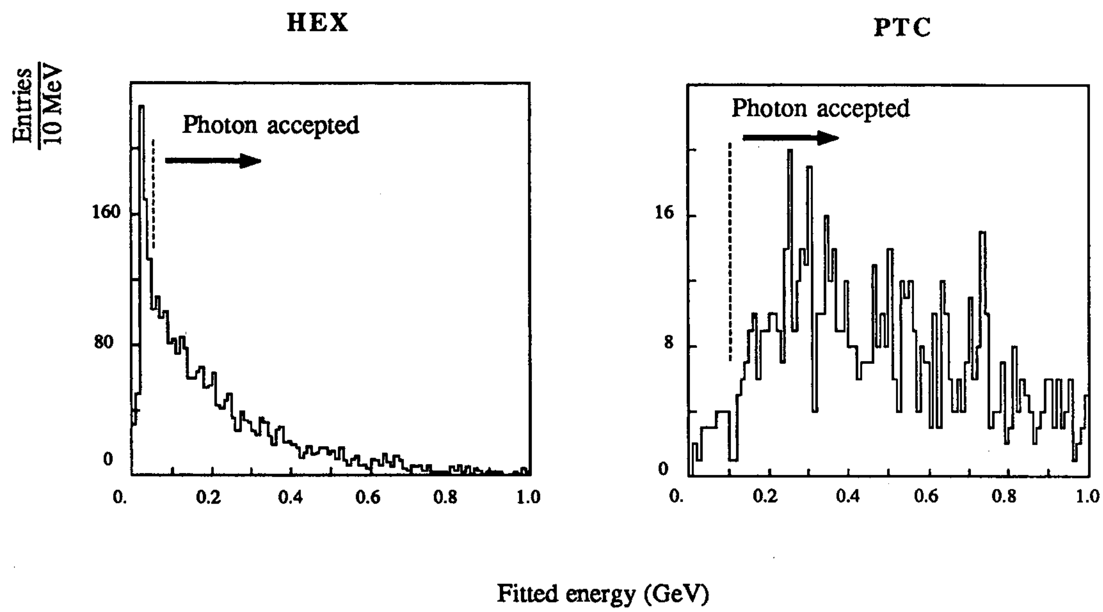

Figure 3.6: Energies of photons after kinematic fit

no-tag 2 photon analyses to require a small $|\sum \vec{p}\,|_{\perp}$ in selecting an exclusive final state.

Another way to exploit this knowledge of the transverse momentum is to treat the final state X as having a measured $p_x = p_y = 0$, and to apply a fitting procedure utilizing the constraints of energy and momentum conservation. The goodness of fit is then a test of the exclusivity hypothesis which takes into account the errors in the measurement of the particles' momenta. This approach has the added advantage of improving on the measured momenta, for events which are in actuality exclusive. The resulting improved mass resolution for reconstructed states is particularly important in searching for a particle with a narrow width, such as the ω.

The fitting procedure is based on SQUAW [19], a program developed at LBL in the 1960's for bubble chamber work. The SQUAW program is a powerful and versatile tool designed specifically to do fitting with relativistic particles which decay. One of the most important features of the program for this particular application is flexibility in the choice of variables in which to fit. Thus, the charged tracks can be fit in the variables which are actually measured, (azimuth,tan *dip*, and curvature) or (ϕ, s, k), whereas the photons can be fit in $(\phi, s, \ln E)$. Fitting the photons in $\ln E$ is important because the photons have low energies and large energy errors. In this situation, a fit in energy has various pitfalls, among which is the possibility of trial solutions with negative energies. By fitting in $\ln E$ these problems are avoided.

In the set up for the fit, the final state X is treated as a system with unknown energy and unknown p_z, but with p_x and p_y both measured to be 0. The measurement error on p_x and p_y is taken to be 20 MeV/c. This, of course, is not a completely accurate representation of reality since the X system does in fact have some transverse momentum, and this momentum is not measured. Nevertheless, it is a useful approximation as it generally improves on the measured momenta.

Next, the final state is taken to consist of five particles: four charged pions and a π^0, with the π^0 subsequently decaying to two photons. The momenta of the charged pions and the two photons from the π^0 decay are measured, while their masses are known. There are thus 25 variables (24 momentum components along with the energy of the X system) needed to describe the event, of which 20 have been measured. Energy and momentum conservation at the two decay vertices imposes 8 constraints on the system, yielding $20+8-25=3$ constraints overall.

As input, SQUAW needs the measured momenta in the event, the errors on the measured momenta, and the constraint defining relationships among the various 4-vectors. SQUAW then searches the subspace of track variables which satisfy the constraints for the configuration which is closest to the observed track

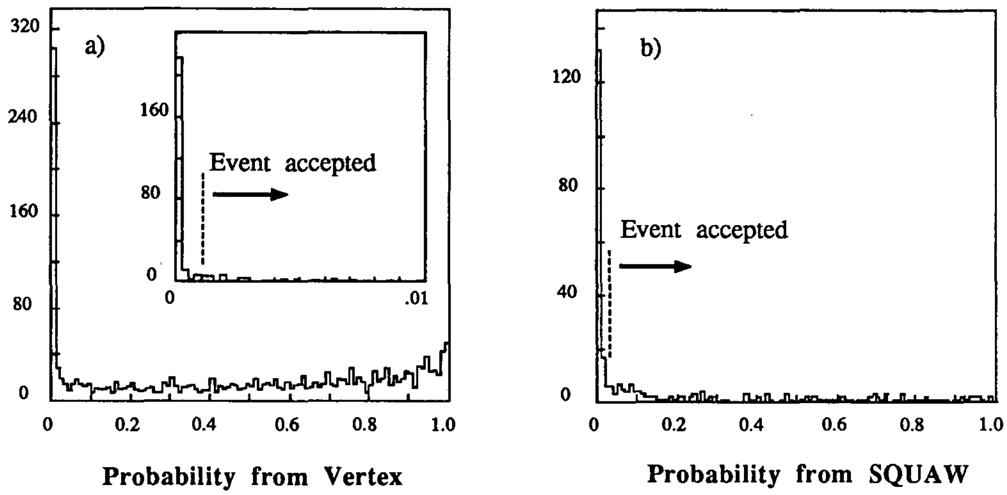

Figure 3.7: Probabability distribution for vertex and SQUAW fits

variables. Closest in this sense is defined by minimizing the chi-squared, $\chi^2_{squaw} = \sum(p_i^{fit} - p_i^{measured})^2/\sigma^2_{p_i}$, where the sum runs over all the measured track variables.

SQUAW needs the best estimate of the track variables and errors at the vertex, but the charged track momenta are measured in the TPC. Therefore, a swimming procedure is used to extrapolate each charged track back to its point of closest approach to the beam. Then the four tracks are fit to a common vertex, yielding the fitted momenta and their errors, to be used as input to SQUAW. The vertex fit also produces χ^2_{vertex}, the chi-squared for the hypothesis that all four tracks originated from a common vertex. The probability of observing a χ^2 value greater than or equal to that actually obtained is required to be greater than .1%, Figure 3.7a.

The energy calibration for photons detected in the calorimeters was based on the observed response of the calorimeters to electrons and positrons (whose energy was also measured in the TPC). In assigning an error to the measured energy, the photons were divided into three categories. The first category consists of photons detected in the HEX which were judged not to have converted prior to entering the HEX, these photons were assigned an energy error of $(\delta E)^2 = (.17)^2 E$, where E is in GeV. For HEX photons which converted in the coil, a floor was added in quadrature so that $(\delta E)^2 = (.17)^2 E + (.135)^2$. For the PTC, energy errors were assigned as $(\delta E)^2 = (.14)^2 E + (.1)^2$.

If SQUAW can converge to a stable solution, it will return the fitted track variables and a chi-squared for the fit overall, χ^2_{squaw}. The probability of observing a χ^2 value greater than or equal to χ^2_{squaw} is required to be greater than 3%, Figure 3.7b.

Finally, the events are required to have satisfied the two ripple trigger described in Section 2.2.5 . This cut is imposed to ensure a reliable simulation of the trigger, Section 4.2.4 . Table 3.1 summarizes the cuts and the number of events surviving at various stages.

As a demonstration of the utility of the kinematic fit, its effect on the $\gamma\gamma$ mass spectrum is presented in Figure 3.8. For this purpose, the events were subjected to a 2 constraint fitting procedure using the constraints of p_x and p_y balance, but making no requirements on the $\gamma\gamma$ invariant mass. The $\gamma\gamma$ mass spectrum is plotted for those events which pass the fit, showing both the raw mass distribution and the mass distribution after the fit. In addition, both spectra have been fit to a Gaussian with a background. Before the kinematic fit the Gaussian fit to the π^0 has a σ of 36 MeV/c^2, whereas after the kinematic fit the σ is 23 MeV/c^2, indicating a considerable improvement in mass resolution. Furthermore, the kinematic fit has pushed some of the low mass background up to higher masses, enabling a clearer separation of the π^0 signal from the background. Finally, Figure 3.9 shows the result of applying a 2 constraint fit

Selection Stage	Events Surviving
Trigger	$\sim 5,000,000$
Preanalysis	$\sim 3,000,000$
Two photon selection	$\sim 1,000,000$
Charged track and photon cuts:	
Require exactly 4 tracks, charge balance	37,989
Require for each track:	
Not in conversion pair	
If $\chi^2_{pi} > 16$, then $\chi^2_{el}, \chi^2_{mu}, \chi^2_{ka}, \chi^2_{pr} > 4$	
Vertex cut: 3 cm in x-y, 8 cm in z	14,046
Require $\mid \sum \vec{p}_{charged} \mid_{\perp} > 80\, MeV/c$	10,999
Photons: only HEX and PTC used	
HEX track association at 24^0	
HEX merging at 15^0	
PTC track association at 8^0	
PTC merging at 10^0	
Require exactly 2 good photons	1971
Kinematic fitting:	
Probability(χ^2_{vertex}) > .001	
HEX photons:	
$\mid y_{hex} \mid < 75\, cm, \mid z_{hex} \mid < 180\, cm$	
$E_{fitted} > 50\, MeV$	
PTC photons:	
$35\, cm < r_{ptc} < 80\, cm$	
$E_{fitted} > 100\, MeV$	
Probability(χ^2_{squaw}) > .03	151
Require 2 ripple trigger	137

Table 3.1: Number of events at various selection stages

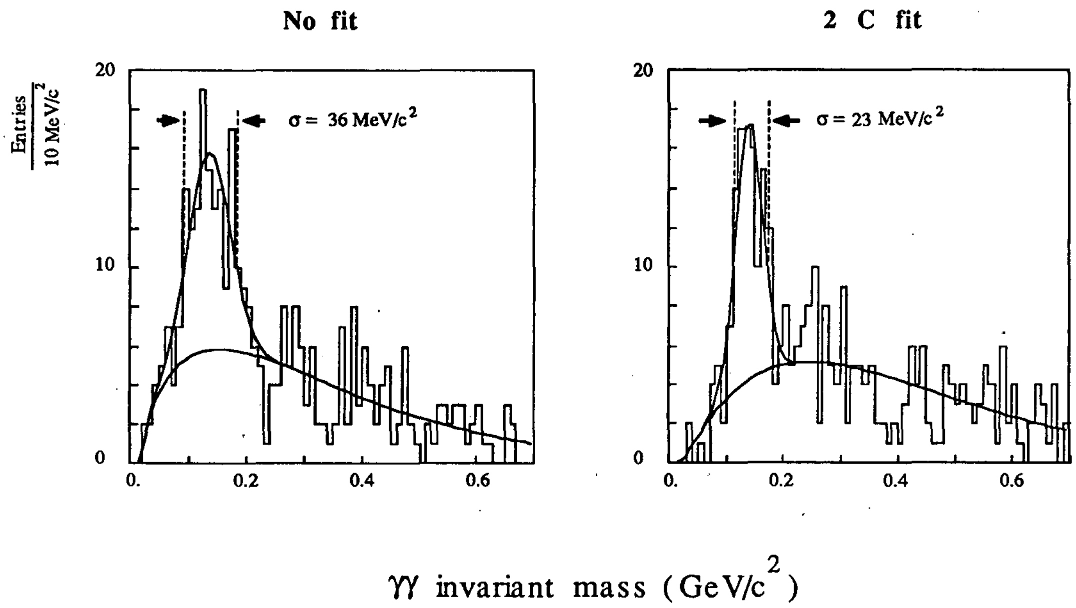

Figure 3.8: $\gamma\gamma$ invariant mass spectrum before and after fit

to events with 3 photons (there are 3 entries per event since there are 3 ways to pick the pair of photons). In contrast with the corresponding spectrum for events with 2 good photons, there is little evidence for π^0 production.

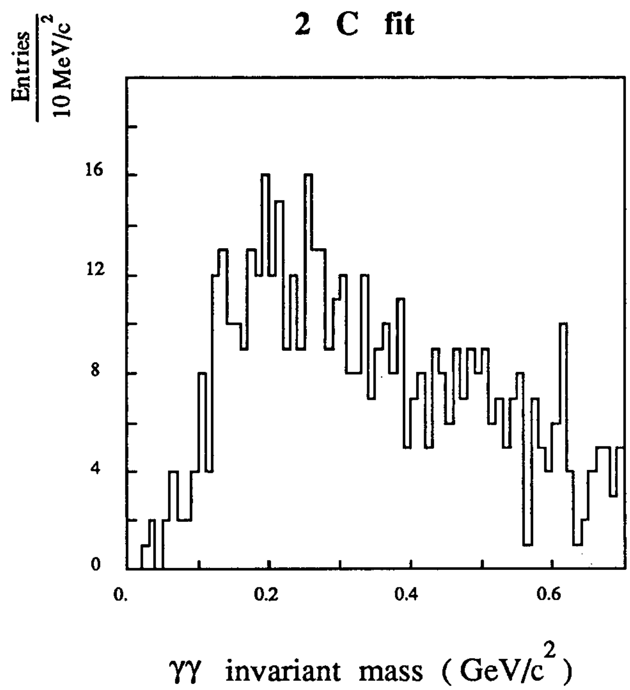

Figure 3.9: $\gamma\gamma$ invariant mass spectrum after fit for events with 3 photons

Chapter 4

Simulation

Of all the photon photon interactions which result in a $\rho^0\omega$final state, only a small fraction are completely reconstructed in the PEP-4 detector system. Therefore in obtaining the cross section $\sigma_{\gamma\gamma\to\rho\omega}$, a correction must be applied to account for the $\rho^0\omega$ events lost due to detector inefficiency. The method used to relate the number of $\rho^0\omega$ events which are reconstructed to the number of $\rho^0\omega$ events actually produced is the subject of this chapter.

The complex process of producing a $\rho^0\omega$ state with a subsequent decay to $\pi^+\pi^-\pi^+\pi^-\pi^0$, coupled with a complicated detector response rules out an analytic approach to this problem. Instead, knowledge of the $\gamma\gamma$ production mechanism and the detector characteristics is used to perform a computer simulation of the processes of $\rho^0\omega$ event generation and reconstruction. To model variables of a statistical nature, such as energies of decay products or detector resolutions, the programs use probability distributions in conjunction with a random number generator. Hence the name Monte Carlo, which is commonly used to indicate this type of simulation.

The simulation is logically divided into two steps, event generation and detector simulation. The event generation, described in Section 4.1, is the process of generating the 4-vectors of the two interacting photons according to the kinematics of 1.1.2, then decaying the $\gamma\gamma$ system to $\rho^0\omega$, finally decaying the ρ^0

and ω according to the known branching ratios. The detector simulation then models the response of the detector to the $\pi^+\pi^-\pi^+\pi^-\pi^0$ final state. This process is discussed in detail for the relevant detector subsystems in Section 4.2 .

4.1 Event Generation

A simulation of a photon-photon interaction must begin with a choice of the 4-vectors of the two interacting photons. The generator [20] used for this analysis is based on the Equivalent Photon Approximation of Section 1.1.2 . As previously mentioned, this means that the photons are considered to be real, with azimuthal symmetry, and that any q^2 dependence is ignored. The simplicity and speed of the EPA generator make it quite suitable for this no-tag analysis. Since the EPA method does involve some approximations, however, this generation method was checked against an 'exact' generator as discussed below.

The EPA generator begins by choosing photon energies according to the spectrum $N(\omega, \theta_{max})$ in equation 1.19. The forward detectors are not used in for this analysis, hence θ_{max} is taken to be 200 mrad, corresponding to the inner radius of the PTC. Since in the EPA the photons are considered to be real, a transverse momentum for the $\gamma\gamma$ system must somehow be added. This is done by using an ansatz for the beam electron scattering. The electrons are scattered at an angle θ from the beam according to $dN/d\theta = constant/\theta$, with a low angle cutoff and a high angle steepening which is dependent on $W_{\gamma\gamma}$. Conservation of momentum then determines the photon 4-vectors.

Since the transverse and longitudinal momentum of the $\gamma\gamma$ system are important in subsequent stages of the simulation, the accuracy of the EPA generation technique was checked against a slower, but more accurate, Vermassern generator [20,21]. The Vermassern program uses the (QED calculable) matrix element for $e^+e^- \rightarrow e^+e^-\gamma\gamma \rightarrow e^+e^-\mu^+\mu-$ to generate a $\mu^+\mu-$ final state. Comparison of various distributions, including $W_{\gamma\gamma}$, transverse momentum, and longitudinal momentum showed the two generators to be in good agreement [22].

Having formed the $\gamma\gamma$ state, it must next be decayed to the particles seen in the detector. In the case of a $\rho^0\omega$ final state, the momenta of the ρ^0 and ω are found by decaying the $\gamma\gamma$ state according to two body phase space. The ρ^0 is then decayed to $\pi^+\pi^-$ according to phase space, with the ρ^0 mass chosen using a P wave Breit-Wigner. The ω is decayed according to the known branching ratios, with $\omega \rightarrow \pi^+\pi^-\pi^0$ 90% of the time. In this case a matrix element of the form $|\mathcal{M}|^2 = |\vec{p}_{\pi^+} \times \vec{p}_{\pi^-}|^2$ is used to decay the ω, with the ω mass again being chosen with a Breit-Wigner. The final states $\omega\pi^+\pi^-$, $\rho^0\pi^+\pi^-\pi^0$, and $\pi^+\pi^-\pi^+\pi^-\pi^0$ are also simulated, using three, four, and five body phase space respectively.

4.2 Detector Simulation

The programs which have been written to model the PEP-4 detector system can be divided into two general categories- slow Monte Carlo and fast Monte Carlo. The slow Monte Carlo routines simulate the various detector systems in detail. In the slow Monte Carlo simulation of the TPC, charged particles are tracked through the TPC, producing individual pad and wire hits which are then put into the raw data format. The offline analysis routines described in the previous chapter can then be applied to this data in the same way the real data is processed. For the calorimeters, the slow Monte Carlo uses an EGS (Electron Gamma Shower) [23] routine to model the development of electromagnetic showers. Again, individual wire signals are produced in the raw data format which can be processed by the calorimeter analysis programs. Though it provides the most accurate detector simulation available, the slow Monte Carlo is aptly named. Since CPU time is a limited resource, the use of this simulation is generally limited to specific studies of detector response and software performance.

In the determination of an overall reconstruction efficiency for a physics process, large numbers of events must be generated to minimize statistical errors. This dictates the use of a reasonably fast simulation, hence the development of a fast Monte Carlo (FMC) utility. The FMC uses a simplified model of the materials in the PEP-4 detector, together with parameterizations of detector response, to perform a simulation much faster than that of the slow Monte Carlo. This simulation, though it bypasses the raw data and subsequent analysis programs, has been found to be a good description of the overall performance of the detector. The methods used by the FMC to simulate the detector elements used in this analysis are described in the following subsections.

4.2.1 TPC Simulation

The simulation of the TPC begins with a choice of the event vertex. In order to account for the finite size of the bunches in the PEP ring, the position of the event vertex is smeared according to the observed vertex distribution. The simulation then propagates the primary particles from the EPA generator outwards from this point through the TPC.

The materials of the beam pipe, pressure wall, field cages, and TPC are modeled as a series of regions in the shape of concentric 'cylinders', each region having a density corresponding to that of the material at that radius. The 'cylinders' are not actually circular in cross section, but rather a hexagonal geometry is used. This is to accommodate the definition of the space between pad rows as a region. When a particle impinges on a region, the likelihood of the particle having a decay or interacting while traversing the region is assessed. If a decay or interaction occurs (based on comparison of the likelihood to a random number in the range 0-1), the products are added to a buffer and subsequently stepped through the detector. This process continues until all particles have either stopped or exited the TPC. Once a particle reaches the boundary of the TPC the tracking process is terminated, thus the FMC does not simulate, for instance, particles which scatter in the coil and re-enter the TPC. For charged particles, the effects of nuclear interactions, multiple scattering, average energy loss, and bremsstrahlung are included. Photon conversions and hadronic interactions for neutrons are also simulated.

Space points are next generated for charged tracks at the points where they cross pad rows. These points are then smeared and fit to a helix to provide a TPC momentum for use in the dE/dx simulation discussed below. A vertex fit is also done for each track using the vertex point chosen for the event.

To simulate the dE/dx measurement, a dE/dx error must first be assigned to the track. Since the dE/dx resolution is a function of the number of dE/dx measurements, a number of usable wire signals must be determined for each track. The maximum number of wire signals is given by the total number of wires the particle's trajectory crosses. The effects of overlapping tracks, delta rays, and dead electronics channels are then subtracted from this maximum number to obtain a number of usable measurements, and hence a dE/dx error. The theoretical dE/dx value for the particle is then smeared by this error to obtain the simulated dE/dx measurement. The simulated dE/dx and TPC momentum are then used by the particle identification algorithm of Section 3.1.4 to produce χ^2's for the various particle hypotheses.

4.2.2 HEX Simulation

When the TPC tracking routine has propagated a particle to the edge of the TPC volume, it stores the particle's momentum and exit position in a buffer, to be used by subsequent simulations. The HEX portion of the simulation begins by selecting photons from this buffer to produce the hits seen in the calorimeter.

Although charged tracks should also produce hits, this effect is not presently simulated.

Having selected a set of photons, the first task is to decide which photons convert in the coil. This is handled by modeling the coil as a slab of aluminum and running an EGS simulation for each photon to determine whether it converts, and if it does, how much energy is lost in the coil. Due to ODC inefficiency, photons which are found to convert are only flagged 90% of the time.

The next step of the simulation takes the energy which reaches the HEX and smears it in $\ln E$, according to $\delta(\ln E) = .17/\sqrt{E}$ (E in GeV). The smearing in $\ln E$ is used, as in the case of the kinematic fit, because of the difficulties associated with low energy photons which have large errors. If a photon has been flagged as converted by the ODC, the photon's energy is increased to account for energy lost in the coil, as in Section 3.1.5. This yields the final energy assigned to the photon. At this point the direction of the photon's momentum is also smeared. This is done by smearing the angles between the photon direction and the x,y, and z axes, each angle being smeared according to $\delta(\theta) = 10$ milliradians

A decision as to whether a given photon is actually reconstructed must next be taken. This decision is based on a curve of reconstruction efficiency as a function of energy deposited in the HEX, known as 'intrinsic efficiency', Figure 4.1. This efficiency is derived from the EGS based slow Monte Carlo for the HEX. The accuracy of the slow Monte Carlo simulation at low energies was checked using a sample of $e^+e^- \rightarrow e^+e^-e^+e^-$ events. This process provides a source of low energy electrons whose momentum can be measured in the TPC. The electrons can then be extrapolated to the HEX and matched to showers found by the reconstruction routines. In this way a curve of reconstruction efficiency vs. TPC momentum is measured for the electrons. Next, the HEX response to low energy electrons is

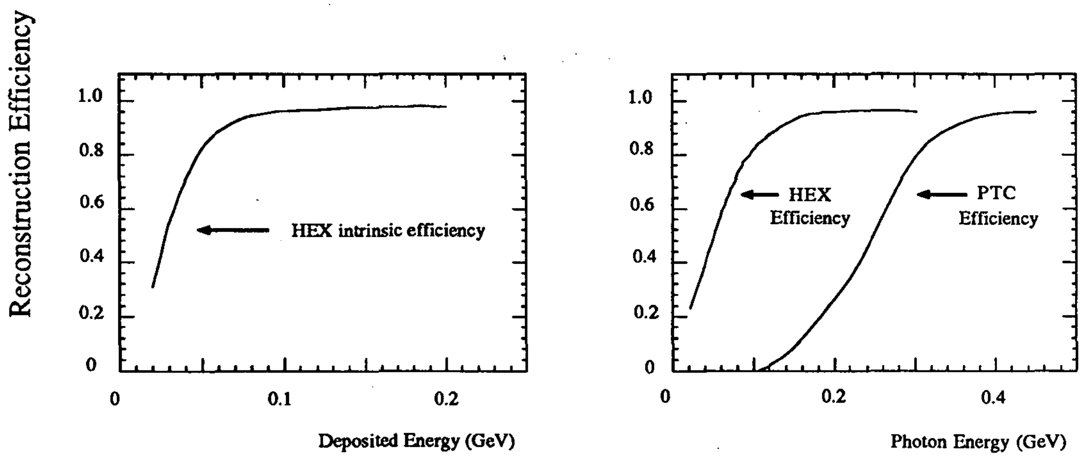

Figure 4.1: Intrinsic efficiency for the HEX, and average photon detection efficiency for both the HEX and PTC

simulated using the slow Monte Carlo and the resulting efficiency as a function of TPC momentum is compared to that found in the data, Figure 4.2. The agreement is quite good, lending credence to the slow Monte Carlo simulation.

Finally, the effects of cluster merging and track association are simulated, using the same cuts used in the offline analysis.

4.2.3 PTC Simulation

The simulation of the PTC is very similar to that of the HEX, with a few minor alterations. The biggest difference between the two simulations is that there is no equivalent of the coil simulation in the PTC routines. This is because there is only a small amount of material (basically, the sector backplanes) between the TPC volume and the PTC. The photon energy and direction smearing is done as in the HEX, using $\delta(\ln E) = .14/\sqrt{E}$ and $\delta(\theta) = 10$ milliradians for resolutions.

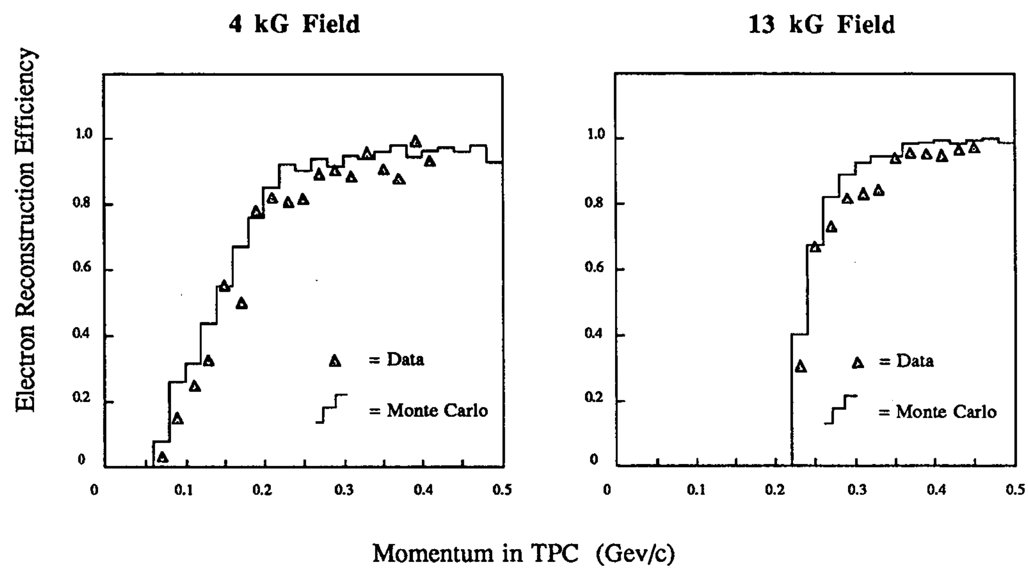

Figure 4.2: Comparison of measured and simulated low energy electron efficiency, for both low field and high field data

Again, an efficiency curve is used to decide which photons are reconstructed. As can be seen from Figure 4.1, the PTC photon efficiency drops off very quickly at low energies. This is probably a consequence of the fact that a shower must penetrate at least three layers to be reconstructed.

4.2.4 Trigger Simulation

Since the $\pi^+\pi^-\pi^+\pi^-\pi^0$ final state is one of relatively low multiplicity, involving primarily low energy particles, it may be anticipated that the efficiency for triggering in such events is significantly less than unity. Therefore an accurate simulation of the trigger is essential for a reliable determination of the overall detector efficiency.

The trigger simulation [24] begins by generating the raw hits in the various detector subsystems (IDC,TPC,ODC,HEX, and PTC) used by the trigger logic. Where necessary, detector effects of a statistical nature (coil penetration probability for charged tracks, latching inefficiencies, etc.) were measured and parameterized for the simulation. The raw hits are then processed by routines which simulate the electronics logic in detail (including timing windows, propagation delays, and latching inefficiencies) to produce the pretrigger and trigger decisions. The trigger simulation has the capability of running either on Monte Carlo generated events or data events, requiring as input the vertex momenta of the reconstructed particles.

The ability of the simulation to run on data considerably facilitates the debugging process, as one can run on a large sample of data events and compare the results of the simulation to the actual performance of the trigger on an event by event basis. This allows problems in the simulation to be efficiently isolated and corrected. Of course, perfect agreement between simulation and data can never be expected on an event by event basis due to processes of a statistical nature (decays, coil penetration, etc.) but the agreement can be verified in an average sense. The simulation of the two ripple trigger was extensively checked through such comparisons.

As a final verification of the simulation for event topologies similar to that of the $\pi^+\pi^-\pi^+\pi^-\pi^0$ state, a sample of about 250 $\pi^+\pi^-\pi^+\pi^-$ events was selected from events which satisfied the (independent) single tag trigger used for single tag analyses. Of these 250 events, 169 were found to satisfy the two ripple trigger in the simulation, whereas 166 events were found to have actually satisfied this trigger. This check, together with others, indicate the trigger simulation is quite accurate.

Chapter 5

Results

In this, the final chapter, the method used to determine the $\rho^0\omega$ cross section from the data is presented. A discussion of error estimates follows, together with a description of some checks which were performed to verify the reliability of the detector simulation. Finally, the significance of the measured cross section is discussed in relation to other measurements and existing theoretical models.

5.1 Measurement of the Cross Section

The objective of this analysis is to measure, as a function of $W_{\gamma\gamma}$ (the total CMS energy of the $\gamma\gamma$ system), the cross section for the process $\gamma\gamma \to \rho^0\omega$. The cross section is derived from the relationship

$$N_{\rho\omega} = L_{e^+e^-} \int \mathcal{A}(W_{\gamma\gamma}) \frac{d\mathcal{L}_{\gamma\gamma}}{dW_{\gamma\gamma}} \sigma_{\gamma\gamma\to\rho\omega}(W_{\gamma\gamma}) dW_{\gamma\gamma} \tag{5.1}$$

where $N_{\rho\omega}$ is the final number of reconstructed $\rho^0\omega$ events in the data, $L_{e^+e^-}$ is the integrated e^+e^- luminosity, $\mathcal{A}$ is the overall reconstruction efficiency of the detector (or acceptance), $\mathcal{L}_{\gamma\gamma}$ is the luminosity function, and $\sigma_{\gamma\gamma\to\rho\omega}$ is the cross section to be measured.

In this analysis, the production of the $\rho^0\omega$ final state was studied in the range $W_{\gamma\gamma} = 1.25 - 3.0$ GeV. This $W_{\gamma\gamma}$ interval was divided into six bins, with five bins of width .25 GeV spanning the range 1.25-2.5 GeV, the sixth bin covering the region $W_{\gamma\gamma} = 2.5 - 3.0$ GeV. For this measurement, the acceptance and cross section are approximated by their average values in each bin, so that the cross section is obtained from the relationship

$$N_{\rho\omega} = \mathcal{A} L_{\gamma\gamma} \sigma_{\gamma\gamma \to \rho\omega} \tag{5.2}$$

where $L_{\gamma\gamma}$ is the integrated photon photon luminosity.

In the following sections, the determination of $N_{\rho\omega}$, $\mathcal{A}$, and $L_{\gamma\gamma}$ are discussed.

5.1.1 The Number of $\rho^0\omega$ Events

The primary tool used in identifying $\rho^0\omega$ events is a scatter plot of the $\pi^+\pi^-\pi^0$ invariant mass versus the invariant mass of the recoiling $\pi^+\pi^-$ system. Since in a $\pi^+\pi^-\pi^+\pi^-\pi^0$ event there are four different ways of combining the pions, there will be four entries per event in such a plot. Any ω production should then be evidenced as an increased density of entries in a vertical band, whereas ρ^0 production should show up in a horizontal band, as illustrated in Figure 5.1. The ρ^0 and ω bands can be used to divide the scatter plot into four different regions, as in Figure 5.1. Production of the $\rho^0\omega$ final state would then be expected to increase the population of entries in Region 1.

Also shown in Figure 5.1 are projections of the scatter plot on to the $M(\pi^+\pi^-\pi^0)$ and $M(\pi^+\pi^-)$ axes, for the range $W_{\gamma\gamma} = 1.25 - 2.25$ GeV. The histograms represent the observed data, while the superimposed curves are from Monte Carlo simulation and will be discussed in detail below. Two projections on to the $M(\pi^+\pi^-\pi^0)$ axis are shown, one histogram showing all entries in the scatter plot, and one histogram where the recoiling dipion mass has been required to fall within the ρ^0 band. An ω signal is evident in both histograms, and appears to be somewhat enhanced by imposing the ρ^0 requirement. Also shown is the projection of all entries on to the $M(\pi^+\pi^-)$ axis, exhibiting a possible enhancement in the ρ^0 region.

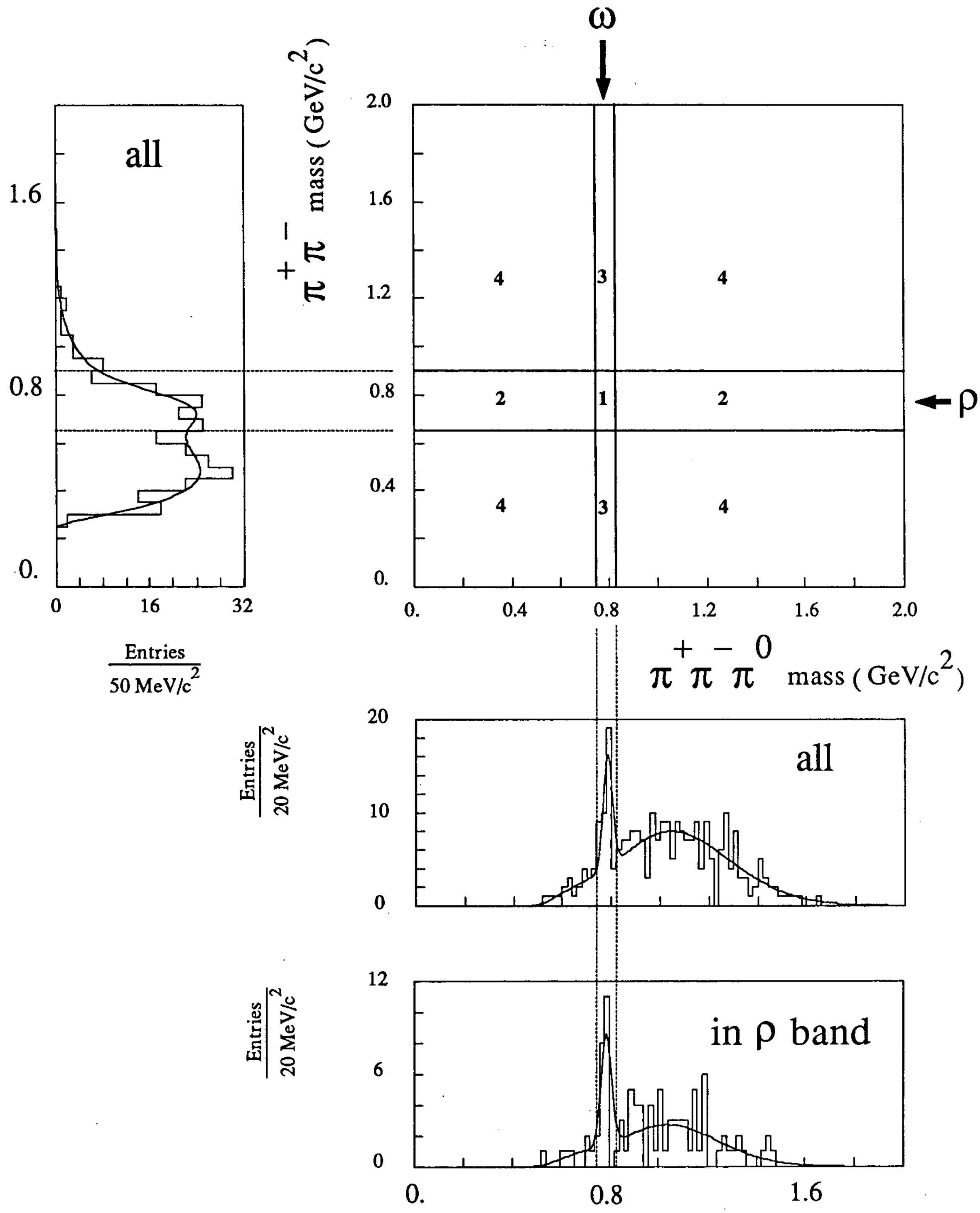

Figure 5.1: Projections of the $M(\pi^+\pi^-)$ vs. $M(\pi^+\pi^-\pi^0)$ scatter plot.

To determine the fraction of events in the final data sample which are due to $\rho^0\omega$ production, the data was modeled as having contributions from four processes: $\rho^0\omega$ production, ρ^0 with non resonant $\pi^+\pi^-\pi^0$ production, ω with non resonant $\pi^+\pi^-$ production, and a $\pi^+\pi^-\pi^+\pi^-\pi^0$ state produced according to five body phase space. The extent to which these four processes are represented in the data is determined by taking mixtures of Monte Carlo events from the four processes, and attempting to mix them together so as to best reproduce the invariant mass distributions observed in the data.

Specifically, the method uses a maximum likelyhood fitting technique to best match a mixture of Monte Carlo events to the observed distribution of entries between the four regions of the invariant mass scatter plot. The number of entries observed in region i is assumed to be distributed according to a Poisson around a 'true' or theoretical value T_i. Then the probability to observe N_i entries in region i will be

$$\mathcal{P}_i = \frac{e^{-T_i} T_i^{N_i}}{N_i!} \tag{5.3}$$

Defining f_X as the fraction of events in the data due to process X, and defining α_X^i as the fraction of entries in region i for process X (determined from Monte Carlo), we expect that

$$T_i = (\alpha^i_{\rho\omega} f_{\rho\omega} + \alpha^i_{\rho 3\pi} f_{\rho 3\pi} + \alpha^i_{\omega 2\pi} f_{\omega 2\pi} + \alpha^i_{5\pi} f_{5\pi}) N_{total} \tag{5.4}$$

where N_{total} is the total number of entries in the scatter plot. At this point, one could just set $T_i = N_i$ and invert the resulting matrix to solve for the f's. However, the f's should be constrained to the range 0-1, in addition one would like to have some estimate of the errors on the fractions. Therefore a fit is employed to find the values of $f_{\rho\omega}$, $f_{\rho 3\pi}$, $f_{\omega 2\pi}$, and $f_{5\pi}$ which maximize the product $\prod_{i=1}^4 \mathcal{P}_i$.

To this end, the minimization program MINUIT [25] is implemented. Basically, the MINUIT program takes as its input a function of the four f's (representing a χ^2) and minimizes that function, returning the fit values of the f's and their errors. An approximate χ^2 function was formed by taking $\chi^2 = -2\ln(\prod_{i=1}^{4}\mathcal{P}_i) + constant$ where the constant was chosen so that the χ^2 is 0 when $N_i = T_i$ for $i = 1,4$. The fit was performed constraining the f's to be between 0 and 1, however no constraint was placed on their sum, effectively allowing the overall normalization to float. Appendix A summarizes the input to, and results from, this fitting procedure.

As a check that the fitting procedure does a reasonable job of reproducing the data, a large statistics Monte Carlo sample (roughly 15 times the size of the data) was prepared by mixing together Monte Carlo events from the four processes according to the fit fractions and the $W_{\gamma\gamma}$ distribution observed in the data. The invariant mass distributions from this sample were then fit and scaled to the number of events in the data. The resulting curves, shown superimposed on the histograms of Figure 5.1, generally show good agreement with the data.

Due to the rather narrow width of the ω, the evidence for ω production is clear, despite the low statistics of the data sample. Unfortunately, the ρ^0 is much broader, and hence more difficult to isolate. Figure 5.2 shows the $M(\pi^+\pi^-)$ distribution when the recoiling $\pi^+\pi^-\pi^0$ mass is required to be in the ω band. The curve represents a fit to the analogous distribution from the large statistics Monte Carlo sample mentioned above. The data shows an enhancement in the ρ^0 region, but the signal is less pronounced than in the case of the ω.

This situation considerably diminishes the fit's capability to distinguish between the $\omega 2\pi$ and $\rho^0\omega$ processes. To obtain some estimate of the significance of the $\rho^0\omega$ signal (as opposed to $\omega 2\pi$), a fit was performed in which the fraction of $\rho^0\omega$events was forced to 0. The cost of this constraint was found to be an increase of 8.5 in the overall χ^2 for the fit. As can be seen in Appendix A, the fit results are consistent with the supposition that all the ω's come from $\rho^0\omega$ production,

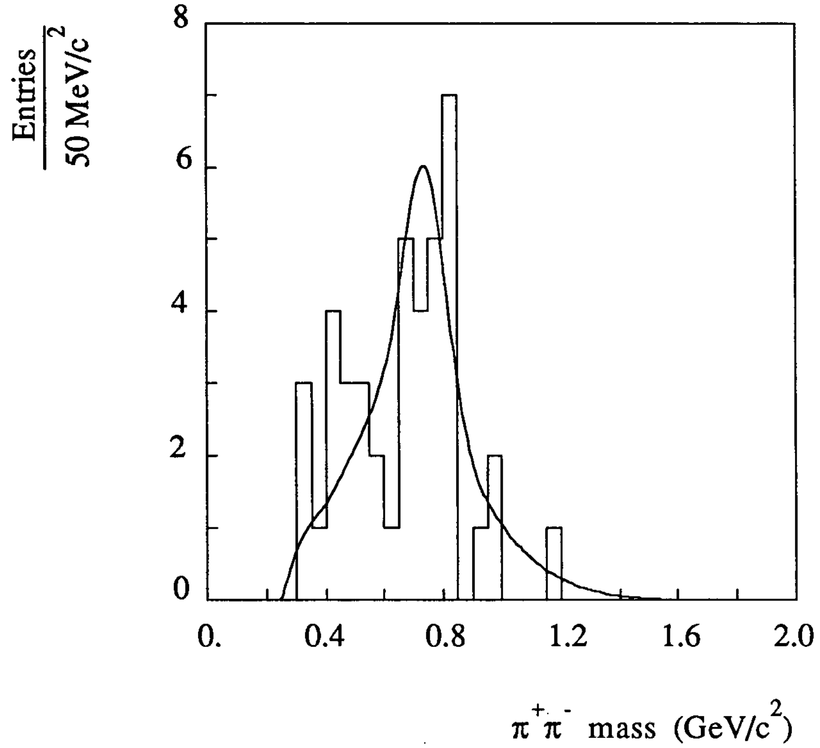

Figure 5.2: The $\pi^+\pi^-$ mass distribution in the ω band.

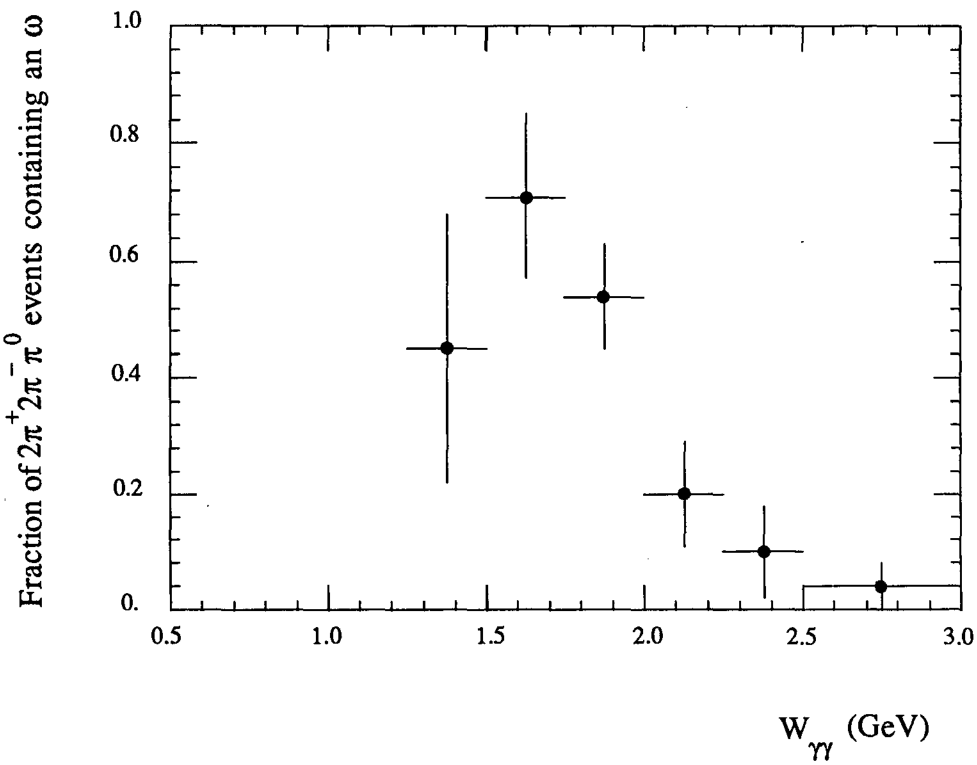

Figure 5.3: The fraction of events with an ω.

and in fact the fit generally favors $\rho^0\omega$ production over $\omega 2\pi$ production. However, with the low statistics of this data sample a definitive separation of the two processes does not seem possible.

In light of this situation, another approach was investigated, in which no attempt is made to distinguish events containing ρ^0's. In this approach fitting is considerably easier, as one needs only distinguish between events with an ω and those without. Accordingly, the scatter plot is divided into only two regions (inside or outside the ω band) and a fit is performed with only two parameters, f_{with} (the fraction of events containing an ω) and $f_{without}$. As expected, the errors on these fractions is much smaller (Appendix A). The fit fraction of events containing an ω is plotted in Figure 5.3, showing that ω production occurs primarily at low $W_{\gamma\gamma}$.

Classification	Events with $W_{\gamma\gamma} < 5$ GeV	Events in $\rho^0\omega$,$W_{\gamma\gamma} < 5$ GeV
Good	67	14
?+	28	5
?-	21	2
Bad	14	0

Table 5.1: Summarized scanning results

To obtain some feeling for the level of background in the final sample, a scan of the 137 events passing all cuts was performed. In particular, events were examined for evidence of extra non-reconstructed tracks or non-reconstructed photons (indicating 'feed down' from higher multiplicity events) or evidence of track associated photons ('feed up'). To summarize the results of the scan, events were divided into four categories: good, ?+ (uncertain, but probably good), ?- (uncertain, but probably bad), and bad. The results of the scan are presented in Table 5.1 for two subsamples of events. One of the subsamples is all events with $W_{\gamma\gamma} < 5$ GeV (there are 7 events above this $W_{\gamma\gamma}$, of which 6 were judged to be Bhabha's), the other subsample was chosen by further requiring that the event have an entry in the $\rho^0\omega$ region (Region 1) of the invariant mass scatter plot. Of the 35 events classified as bad or ?- in the first subsample, 23 were attributed to feed down, while 12 were attributed to feed up.

As can be seen from Table 5.1, the invariant mass requirements used to select the second subsample result in a relatively clean sample of events. Since none of these events were identified as definitely being bad, and since the fitting procedure allows for entries in this area from processes other than $\rho^0\omega$ production which might well model background (such as $\pi^+\pi^-\pi^+\pi^-\pi^0$ produced according to phase space), no explicit correction is applied to the cross section to account for background. Table 5.1 would indicate that background should contribute no more than about 10% to the number of $\rho^0\omega$ events found in the data.

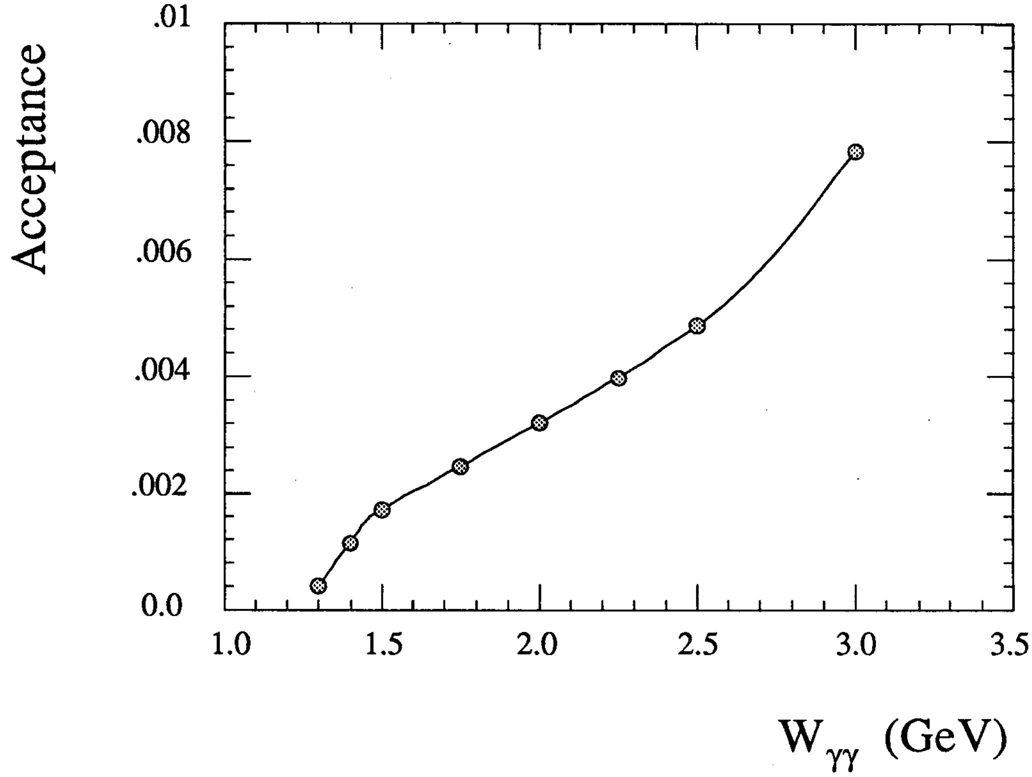

Figure 5.4: The acceptance for $\rho^0\omega$ events.

5.1.2 Acceptance

The detector acceptance is obtained by running Monte Carlo generated $\rho^0\omega$events through the full detector simulation, applying the selection criteria of Chapter 3, and determining the ratio of the number of events surviving the selection cuts to the total number of events generated. This ratio defines the acceptance, $\mathcal{A}$, and is plotted in Figure 5.4. The acceptance was measured at eight points, indicated by the circles in the plot.

As previously mentioned in Chapter 4, the detector simulation is not quite complete in that the TPC simulation does not account for backscatters at the edges of the TPC volume, and the calorimeter programs do not simulate the deposition of energy in the calorimeters by charged tracks. A correction of about 20% to the acceptance is needed to account for these effects, detailed further in

Section 5.1.4. This correction has been applied in Figure 5.4.

5.1.3 Luminosity

As indicated in Section 1.1.1, the integrated photon-photon luminosity in a given $W_{\gamma\gamma}$ range, $L_{\gamma\gamma}$, is related to the integrated e^+e^- luminosity, $L_{e^+e^-}$, by

$$L_{\gamma\gamma} = L_{e^+e^-} \int \frac{d\mathcal{L}_{\gamma\gamma}^{TT}}{dW_{\gamma\gamma}} dW_{\gamma\gamma} \tag{5.5}$$

where the integral is over the $W_{\gamma\gamma}$ range in question. While the integral over $W_{\gamma\gamma}$ can be handled via numerical integration, obtaining an accurate estimate of $L_{e^+e^-}$ is less straightforward. The TPC detector is a large and complicated system, as is the offline processing structure, so that the task of determining how much 'good' (i.e. all systems functioning properly, no problems in offline processing or databases) data was obtained is not trivial. A fairly involved investigation of this subject [26] yielded the conclusion that $L_{e^+e^-}$ for the data set of this analysis is 64 pb^{-1}, with an estimated error about 10%.

5.1.4 Corrections

In Section 3.2.2, it was argued that the loss of good events due to fake photons from charged tracks should be less than about 20%. This estimate was obtained through studying the $\pi^+\pi^-\pi^+\pi^-$ final state, which is quite similar in topology to the $\pi^+\pi^-\pi^+\pi^-\pi^0$ state which is the subject of this analysis. To obtain a more quantitative estimate of this factor, a $\pi^+\pi^-\pi^+\pi^-$ event sample was selected using essentially the charged particle selection criteria of Section 3.2.1. These events were then divided into smaller samples, based on the number of 'good' photons found in the event. The distribution of $| \sum \vec{p}_{charged} |_\perp$ was then examined for peaking at 0, indicating the production of exclusive $\pi^+\pi^-\pi^+\pi^-$ events. The size of this peak in the sample with 1 good photon was estimated as being 13% the size of the analogous peak in the sample with 0 good photons, indicating a correction factor of about $.13 + (.13)^2$, or 15%. The error on this correction was estimated at about 5%, leading to a correction of $15 \pm 5\%$.

If a charged track undergoes a backscatter outside the TPC volume and re-enters the TPC, it may be found by the tracking routines and added to the list of tracks in the event. Since this effect is not simulated in the Monte Carlo, and since exactly four tracks are required in the data, a correction factor is needed to account for the loss of events due to backscatters. This problem was approached in a rather similar fashion to the method used in correcting for fake photons. Two $\pi^+\pi^-\pi^+\pi^-$ event samples were selected, one with exactly four tracks and one with exactly four 'good' tracks and one 'bad' (non-vertex) track. The $| \sum \vec{p}_{charged} |_\perp$ distributions were examined to determine the relative sizes of the peaks, with the five track sample found to have a peak roughly 8% the size of the peak in the four track sample. However since extra tracks can come from other sources, (decays, beam pipe interactions, etc.) a sample of the five track events was scanned to determine how many of the extra tracks actually came from backscatters. This yielded a correction factor of 5%, with an error of 2%.

To first order, the corrections for extra tracks and for extra photons should be roughly independent, so the overall correction factor is taken to be $(1.15)(1.05) = 1.21$.

5.1.5 Cross Sections

With the previous results, Equation 5.2 can be used to compute cross sections. Two cross sections are presented in this section, $\sigma_{\gamma\gamma\to\rho\omega}$ and $\sigma_{\gamma\gamma\to\omega\pi^+\pi^-}$, where the $\omega\pi^+\pi^-$ final state includes both ρ^0 and non resonant $\pi^+\pi^-$ production. Table 5.2 details the input to Equation 5.2 and the resulting cross sections.

The errors quoted on the cross section at this stage are statistical only, arising from the Poisson fluctuations in the number of events in a $W_{\gamma\gamma}$ bin together with

$W_{\gamma\gamma}$	$\mathcal{A}$	$L_{\gamma\gamma}$ (nb^{-1})	$N_{\rho\omega}$	$N_{\omega\pi^+\pi^-}$	$\sigma_{\gamma\gamma\to\rho\omega}$ (nb)	$\sigma_{\gamma\gamma\to\omega\pi^+\pi^-}$ (nb)
1.25-1.50	.00087	215.	2.2	1.8	11.8 ± 9.7	9.6 ± 6.9
1.50-1.75	.00211	170.	5.9	8.5	16.4 ± 12.1	23.8 ± 8.2
1.75-2.00	.00285	136.	14.6	14.0	37.6 ± 14.5	36.1 ± 9.3
2.00-2.25	.00360	113.	0.0	4.8	0.0 ± 7.0	11.8 ± 5.9
2.25-2.50	.00443	95.	0.4	1.8	0.9 ± 7.0	4.3 ± 3.5
2.50-3.00	.00637	150.	1.7	1.1	1.8 ± 1.5	1.2 ± 1.2

Table 5.2: Cross sections for $\rho^0\omega$ and $\omega\pi^+\pi^-$

the fitting errors on the fractions. An analysis of the systematic errors will be presented in the next section.

The cross sections of Table 5.2 are also plotted in Figure 5.5. The $\rho^0\omega$ and $\omega\pi^+\pi^-$ cross sections are consistent with one another, however, the $\rho^0\omega$ cross section has much larger errors due to correlations with the $\omega\pi^+\pi^-$ ($\pi^+\pi^-$ produced according to phase space) process. It is consistent with the data to assume that all the ω's are produced with a ρ^0, therefore the better determined $\omega\pi^+\pi^-$ cross section is used as an estimate of the $\rho^0\omega$ cross section in Sections 5.3 and 5.4.

5.2 Systematic Errors

Probably the largest single source of systematic error for this measurement is uncertainty in the photon detection efficiency of the calorimeters. As indicated in Section 4.2, these efficiencies were checked by studying the low energy electron detection efficiency, but a 10% (absolute) error in the intrinsic efficiency probably cannot be ruled out by these checks. Since two photons must be detected in the final state, a 10% error in intrinsic efficiency is likely to be compounded into a somewhat larger error for the overall acceptance. In fact, Monte Carlo simulation indicates that such a change in intrinsic efficiency translates to about a 20% change in the overall acceptance, leading to an estimate of 20% for the systematic error due to uncertainty in the photon efficiency.

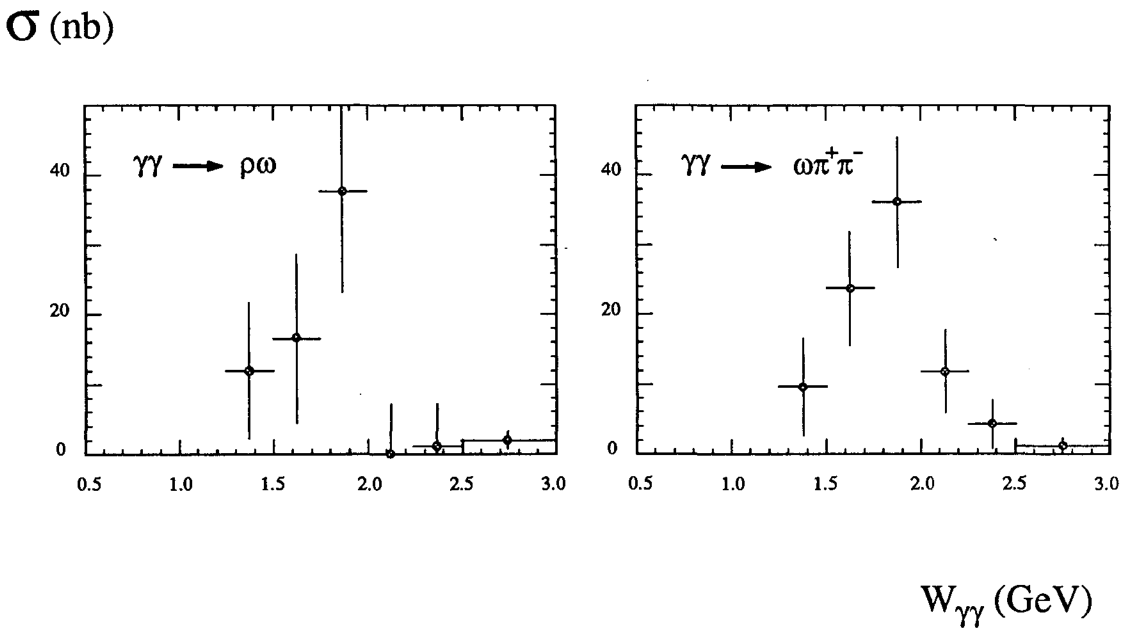

Figure 5.5: Cross sections for $\rho^0\omega$ and $\omega\pi^+\pi^-$. Errors are statistical only.

Another source of error in the acceptance is in the efficiency for finding low angle tracks. Comparison of the distributions of track angles from data and Monte Carlo indicate that this effect should contribute no more than 15% to the error in the acceptance.

Charged tracks also play a role in the acceptance through the contribution of the trigger efficiency. As mentioned in Section 4.2.4, the trigger simulation was checked using independently triggered $\pi^+\pi^-\pi^+\pi^-$ events, and was found to agree well with the data, with an error estimated at 5%.

As an overall check of the charged particle simulation, the Monte Carlo was used to estimate the cross section for two photon production of the $\pi^+\pi^-\pi^+\pi^-$ final state at $W_{\gamma\gamma} = 1.5$ GeV, roughly where other measurements have observed the peak cross section [27,28,29]. An exclusive $\pi^+\pi^-\pi^+\pi^-$ sample was selected from the data using essentially the same cuts as those used for the $\pi^+\pi^-\pi^+\pi^-\pi^0$ selection, except that instead of requiring exactly two good photons the events were required to have no more than one good photon. The $|\sum \vec{p}_{charged}|_{\perp}$ distribution from the resulting sample was found to agree quite well with Monte Carlo, indicating little background from non-exclusive events. A final cut requiring $|\sum \vec{p}_{charged}|_{\perp}$ to be less than 100 MeV/c was applied to both data and Monte Carlo, yielding a measured cross section for $\pi^+\pi^-\pi^+\pi^-$ production at $W_{\gamma\gamma} = 1.5$ GeV of 150 nb. This result compares relatively favorably with a previous measurement from the TPC/2γ collaboration of 172 nb [29].

The final contributions to the acceptance uncertainty come from the corrections discussed in Section 5.1.4. The errors from these corrections are taken to be 5% (requirement of exactly two photons) and 2% (requirement of exactly four tracks).

As indicated in Section 5.1.3, the uncertainty on the integrated luminosity is estimated at about 10%. Taking this in quadrature with the acceptance systematics gives an overall systematic error of 28%.

5.3 Comparison to Experiment

At present, there are three other experimental results relevant to this measurement: upper limits on $\sigma_{\gamma\gamma\to\rho\omega}$from the JADE [30] and PLUTO [31] collaborations, and a measurement of $\sigma_{\gamma\gamma\to\omega\pi\pi}$ from the ARGUS [10] collaboration. The PLUTO result is published, while the JADE and ARGUS results are both preliminary.

The upper limits (95% confidence level) on the $\rho^0\omega$ cross section from PLUTO and JADE are shown with the results of this analysis in Figure 5.6. Our result seems to be in mild disagreement with the JADE limits, while the disagreement with the PLUTO result is somewhat more severe.

The ARGUS collaboration has also studied the $\pi^+\pi^-\pi^+\pi^-\pi^0$ final state, and has observed a clear ω signal in the $\pi^+\pi^-\pi^0$ invariant mass distribution. As in

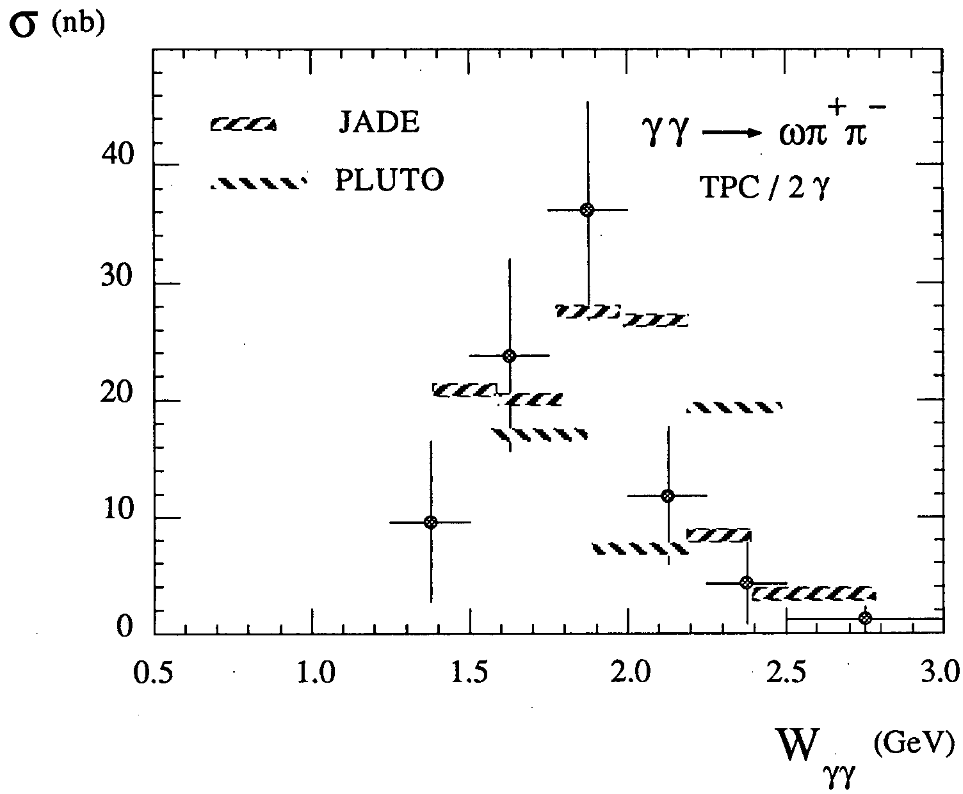

Figure 5.6: Comparison to JADE and PLUTO upper limits.

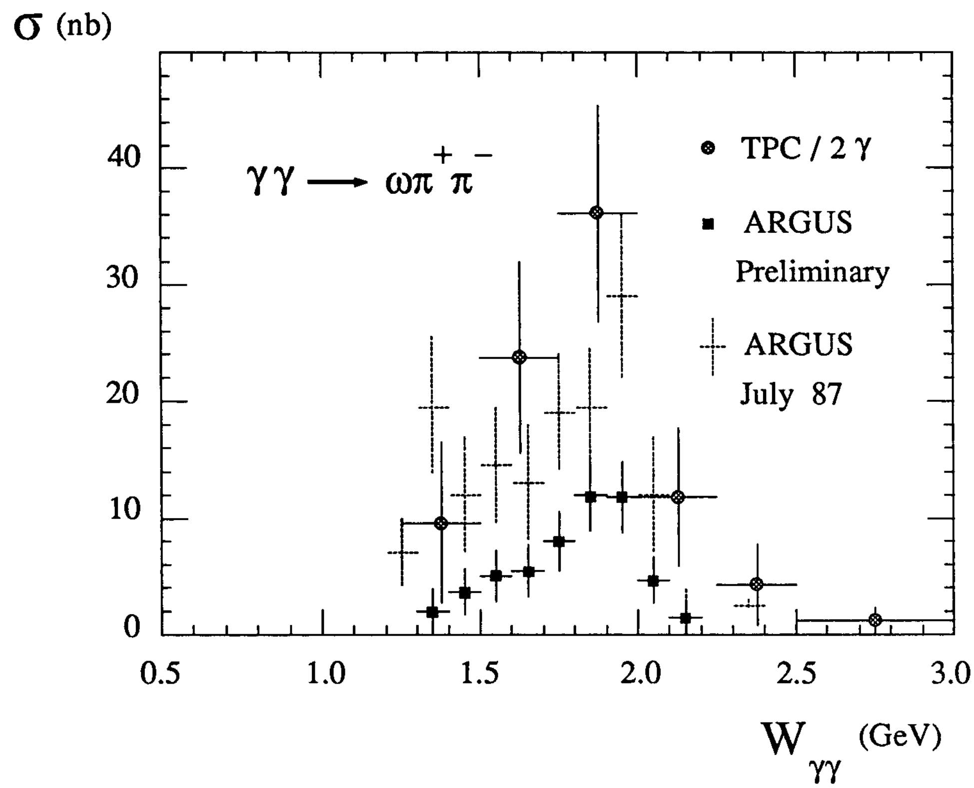

Figure 5.7: Comparison to cross section measured by ARGUS. Errors on both measurements are statistical only. The points with dashed error bars are from a recent conference presentation by ARGUS.

this analysis, ARGUS finds that the recoil $\pi^+\pi^-$ mass distribution indicates a dominant ρ^0 contribution, but they have not separated out the ρ^0 component. They therefore report a measurement of $\sigma_{\gamma\gamma\to\omega\pi\pi}$, which is compared to the same measurement from this collaboration in Figure 5.7.

It is interesting to note that both experiments observe a peaking in the cross section at a $W_{\gamma\gamma}$of about 1.8 GeV, considerably above threshold for $\rho^0\omega$production. However, there seems to be a considerable discrepancy in the magnitudes of the two measurements. This may be partially explained by the use of a $\pi^+\pi^-\pi^+\pi^-\pi^0$ final state produced according to phase space in the acceptance calculation for ARGUS. The acceptance for the TPC detector is considerably different for the $\rho^0\omega$ and $\pi^+\pi^-\pi^+\pi^-\pi^0$ phase space final states; using the $\pi^+\pi^-\pi^+\pi^-\pi^0$ phase space acceptance would change the measured cross section from 36 nb at the peak to about 20-25 nb at the peak. Final resolution of this discrepancy will probably require further measurements by other groups. (Note added in proof: a recent conference presentation by ARGUS [32,33], Figure 5.7, indicates that the two measurements are now compatible.)

5.4 Comparison to Theory

As mentioned in Section 1.2.3, there have been a number of explanations suggested to account for the observed peaking of the $\rho^0\rho^0$ cross section near threshold. In this section, the results of this experiment are compared to the predictions from several such models.

5.4.1 Threshold Enhancement Mechanism

Perhaps the simplest way to explain the peaking of the $\rho^0\rho^0$ cross section is to postulate that it is a threshold effect, arising from a smoothly falling matrix element competing with a phase space factor which rises sharply near threshold. This approach has been shown to be quite successful in reproducing the observed $\rho^0\rho^0$ cross section [29]. To investigate the possibility of explaining the $\rho^0\omega$ cross section in the same way, a fit was applied as follows.

The cross section was written as [34]

$$\sigma_{\gamma\gamma\to\rho\omega} = constant \cdot \frac{\mid \vec{p}_f \mid}{W_{\gamma\gamma}^3} \cdot \mid M_{fi} \mid^2 \tag{5.6}$$

where $\mid \vec{p}_f \mid$ is the momentum of the outgoing ρ^0 or ω in the $\rho^0\omega$ CM frame (the ρ^0 and ω widths are neglected in calculating $\mid \vec{p}_f \mid$), and an S-wave Breit Wigner was used for the matrix element $\mid M_{fi} \mid^2$. The cross section was then integrated over the $W_{\gamma\gamma}$ bins and compared to the data. Fits were then performed under various conditions to see if this parameterization of the cross section could reproduce the data.

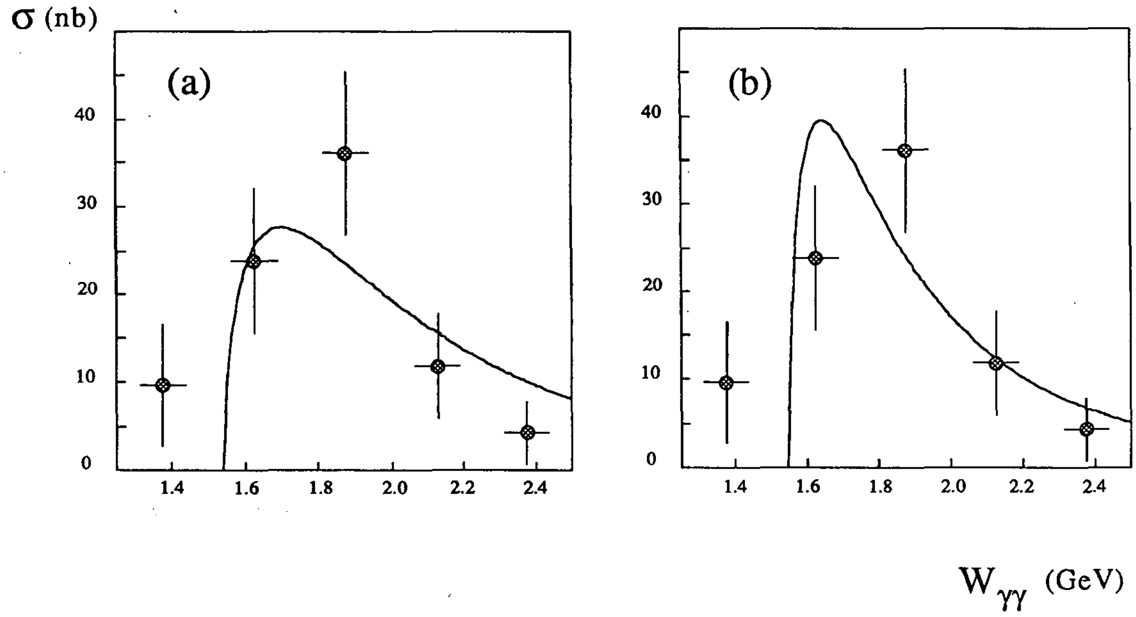

Figure 5.8: Comparison of the data to a threshold enhancement model.

In the first fit performed, both the mass and width used in the Breit Wigner were allowed to vary with no constraints. The best fit was obtained with a mass of $1.76 \pm .04$ GeV/c^2 and a width of $.24 \pm .12$ GeV/c^2.

Next a fit was performed in which the mass was constrained to be very small, .01 GeV/c^2, so as to give the matrix element a $W_{\gamma\gamma}^{-2}$ dependence near threshold. The best fit obtained under these conditions is shown in Figure 5.8a. The $\chi^2/d.o.f.$ for this fit (excluding the lowest data point, since neglecting the ρ^0 width effectively forces the calculated cross section to 0 below nominal $\rho^0\omega$ threshold) was found to be 1.25.

In the final fit, the Breit Wigner width was constrained to be very small, .01 GeV/c^2, and the mass was allowed to vary, so as to allow a more steeply falling matrix element. Under these conditions, the best fit ($\chi^2/d.o.f. = .60$) was obtained with a mass of 1.1 GeV/c^2, and is shown in Figure 5.8b.

These fits indicate that a threshold enhancement effect will not be able to reproduce the shape of the observed cross section. However, because of the large errors on the measured points, such an explanation cannot be ruled out by our data.

5.4.2 Factorization Model

In Section 1.2.3 it was suggested that in the framework of the Vector Dominance Model the reaction $\gamma\gamma \rightarrow \rho^0\rho^0$ should in some sense look like elastic $\rho^0\rho^0$ scattering. The curve in Figure 1.11 is based on such an assumption, wherein the elastic $\rho^0\rho^0$ cross section is estimated using the additive quark model and an extrapolation of higher energy proton-antiproton cross sections [5].

Alexander *et al.* [35,36] have objected to this extrapolation of high energy hadronic cross sections, and suggest instead a model based on factorization. In this scheme the $\rho^0\omega$ cross section should be calculated as

$$\sigma_{\gamma\gamma\rightarrow\rho\omega} = \sum_i \frac{\sigma^i_{p\gamma\rightarrow p\rho} \cdot \sigma^i_{p\gamma\rightarrow p\omega} \cdot F^2_{p\gamma}}{\sigma^i_{pp\rightarrow pp} \cdot F_{pp} \cdot F_{\gamma\gamma}} \tag{5.7}$$

where the summation is over the diffractive (Pomeron exchange) and one pion exchange processes. The F's are flux factors arising from the different masses involved in the calculation. This relation is then applied at fixed $\mid \vec{p}_f \mid$ using photoproduction data to estimate the cross section.

This model has been able to account for the observed $\rho^0\rho^0$ cross section in a reasonable way, and the authors of [36] have also published predictions for the $\rho^0\omega$ cross section. These predictions are reproduced in Figure 5.9 and appear to be inconsistent with the results of this experiment.

5.4.3 Four Quark Models

The observed peak in the $\rho^0\rho^0$ cross section has naturally led to speculations regarding intermediate state resonances. Since in the VDM framework the photon-

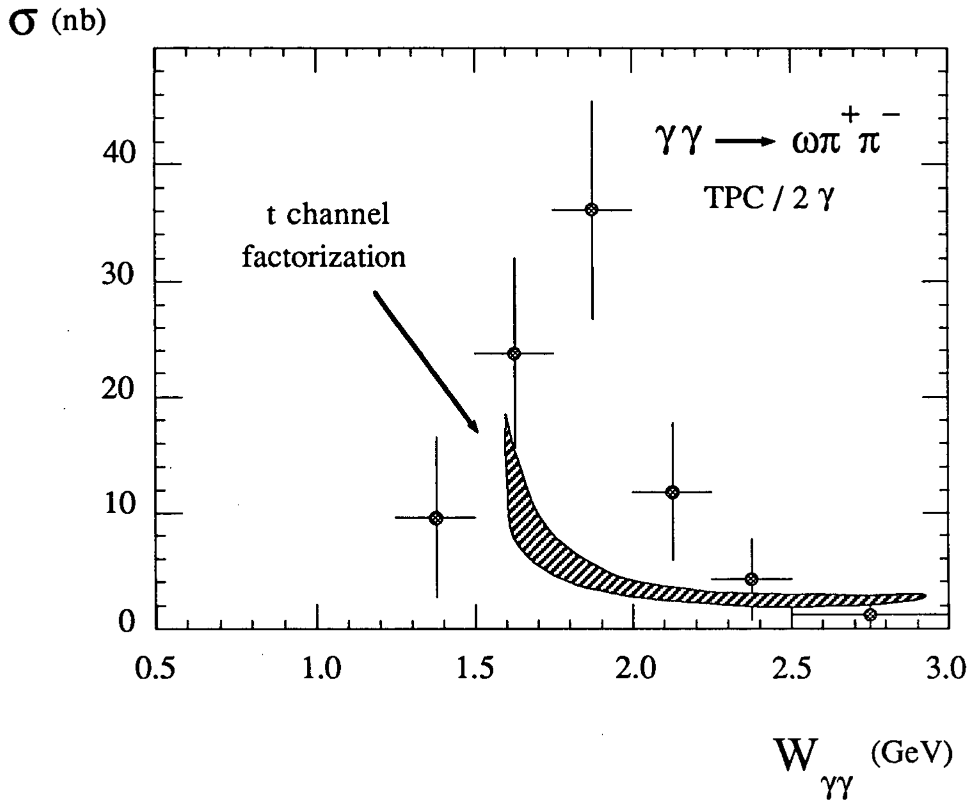

Figure 5.9: Comparison of the data to a factorization model, taken from [36]

photon interaction is viewed as the interaction of virtual vector mesons, and since mesons are composed of quark-antiquark pairs, it is reasonable to suggest that such a resonance would consist of two quarks and two antiquarks. Such four quark bound states were discussed some time ago within the framework of the MIT Bag Model by Jaffe [37,38]. Several authors [39,40,41,42,43] have used the predictions of this model, together with the VDM formalism, to successfully account for the observed $\rho^0\rho^0$ cross section.

The same authors have made predictions regarding the cross sections for the production of other vector meson pairs. The predictions are functions of various parameters which are not precisely known, such as the masses of the relevant four quark states. While predictions for the $\rho^0\omega$ cross section have been published using specific values of these parameters, an effective test of this model requires a fit to the data in which the parameters are allowed to vary.

Achasov *et al.* have published their prescription for the $\rho^0\omega$ cross section in [41], reproduced below:

$$\sigma_{\gamma\gamma\to\rho\omega} = 95 \cdot Y^2 \cdot \frac{F_\rho(s)}{s} \mid \frac{1}{D(m_0,s)} \mid^2 \ nb \tag{5.8}$$

Where

$$F_\rho(s) = \frac{1}{\pi}\int_{4m_\pi^2}^{(\sqrt{s}-m_\omega)^2} dm^2 \frac{m\Gamma_\rho(m)}{\mid D_\rho(m)\mid^2}\rho(s,m_\omega,m) \tag{5.9}$$

$$m\Gamma_\rho(m) = m_\rho\Gamma_\rho\frac{m_\rho}{m}\cdot\frac{q(m)^3}{q(m_\rho)^3}\cdot\frac{1+(Rq(m_\rho))^2}{1+(Rq(m))^2} \tag{5.10}$$

$$q(m) = \frac{1}{2}\sqrt{m^2-4m_\pi^2} \tag{5.11}$$

$$D_\rho(m) = m_\rho^2 - m^2 - im\Gamma_\rho(m) \tag{5.12}$$

$$D(m_0,s) = m_0^2 - s - iY[0.495a_0 + 1.37F_\rho(s)] \tag{5.13}$$

$$\rho(s,m_1,m_2) = \sqrt{s-(m_1+m_2)^2}\cdot\sqrt{s-(m_1-m_2)^2}/s \tag{5.14}$$

with $s = W_{\gamma\gamma}^2$, $R = 2\ \mathrm{GeV}^{-1}$, $m_\rho = .769\ \mathrm{GeV/c^2}$, and $\Gamma_\rho = .154\ \mathrm{GeV/c^2}$. In the above, m_0 is the mass of the four quark state, Y represents a coupling pertaining

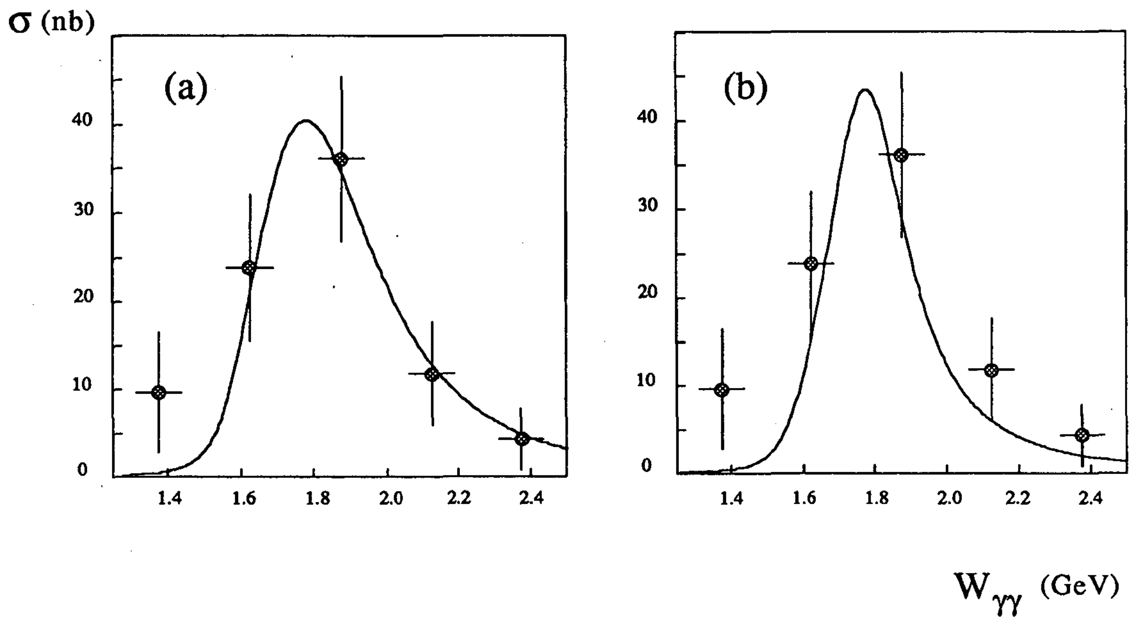

Figure 5.10: Comparison of the data to a four quark model.

to the dissociation of the four quark state into two mesons, and a_0 is a parameter introduced to account for non-calculable contributions to the resonance width.

The above form for the cross section was integrated over $W_{\gamma\gamma}$ bins and compared to the data in a fitting procedure similar to that described in Section 5.4.1. The fit was first performed allowing m_0, a_0, and Y to vary (with a_0 constrained to be non-negative), yielding the result pictured in Figure 5.10a. This fit has $m_0 = 1.85 \pm .06\,\mathrm{GeV/c^2}$, $a_0 = 0 \pm .23$, and $Y = 1.7 \pm .51\,\mathrm{GeV}^2$, with a $\chi^2/d.o.f.$ of .37 . The fit was also performed constraining $Y = 1\,\mathrm{GeV}^2$, as in the predictions of [41]. This fit gave the result pictured in Figure 5.10b, with $m_0 = 1.8 \pm .05\mathrm{GeV/c^2}$, $a_0 = 0 \pm .08$, and a $\chi^2/d.o.f.$ of .88 . On this basis it would appear that a four quark model can be used to account for the observations of this experiment.

5.5 Summary and Conclusions

Since the first observation of the process $\gamma\gamma \to \rho^0\rho^0$ in 1980, there has been considerable interest in understanding the observed peaking of the cross section for this reaction near threshold. This analysis investigates the related process $\gamma\gamma \to \rho^0\omega$ in an effort to further elucidate the mechanism underlying the observed peak in the cross section for $\rho^0\rho^0$ production.

Evidence of $\rho^0\omega$production was sought in the channel $\gamma\gamma \to \rho^0\omega \to \pi^+\pi^-\pi^+\pi^-\pi^0$. A sample of exclusive $\pi^+\pi^-\pi^+\pi^-\pi^0$ events was selected using a 3C kinematic fit, where two constraints come from the requirement of transverse momentum balance and one constraint comes from the requirement that the observed photons reconstruct to a π^0. The fraction of events in the final sample due to $\rho^0\omega$ production was extracted from a scatter plot of the $\pi^+\pi^-$ invariant mass versus the $\pi^+\pi^-\pi^0$ invariant mass, in which each event has four entries. The $\pi^+\pi^-\pi^0$ mass distribution shows clear evidence of ω production, and the mass of the dipion system recoiling against the ω appears to be dominated by ρ^0 production. However, due to the large width of the ρ^0 and the limited statistics of the data, a definitive separation of the ρ^0 component was not possible. The cross section for $\gamma\gamma \to \omega\pi^+\pi^-$ (where the $\pi^+\pi^-$ state includes ρ^0) is therefore presented as the best estimate of $\sigma_{\gamma\gamma\to\rho\omega}$.

Comparison of this result to upper limits on $\sigma_{\gamma\gamma\to\rho\omega}$ from the JADE and PLUTO collaborations shows that our cross section exceeds the PLUTO limits by a substantial margin, while the disagreement with JADE is less severe. Our measured cross section is also considerably larger than a preliminary measurement of $\sigma_{\gamma\gamma\to\omega\pi\pi}$ from ARGUS, though it appears the two experiments may now be in agreement.

Finally, the data are compared to the predictions from several models which have been used to account for the observed $\rho^0\rho^0$ cross section. Our data are inconsistent with a prediction from the factorization approach of Alexander *et al.*, while four quark model of Achasov *et al.* appears capable of accommodating the data with little difficulty. A threshold enhancement model, though apparently incapable of reproducing the shape suggested by the observations, cannot be ruled out at this time.

Appendix A

Fitting

This appendix contains details regarding the fitting procedure used to extract the fractions of various processes in the data.

The four regions in the invariant mass scatter plot are defined by the choice of the ω and ρ^0 bands. The ω band is chosen as the region $M(\pi^+\pi^-\pi^0) = 740-820\,\mathrm{MeV/c^2}$, while the ρ^0 band is chosen as $M(\pi^+\pi^-) = 650-900\,\mathrm{MeV/c^2}$. However, since the lowest $W_{\gamma\gamma}$ bin is below threshold for $\rho^0\omega$ production, the ρ^0 peak should be shifted lower and in this $W_{\gamma\gamma}$ bin the ρ^0 band is chosen as $M(\pi^+\pi^-) = 500-750\,\mathrm{MeV/c^2}$. Table A.1 lists the number of entries found in each region of the data scatter plot.

Tables A.2, A.3, A.4, and A.5 list the expected fractions of events in each region for the four Monte Carlo processes.

$W_{\gamma\gamma}$	N_1	N_2	N_3	N_4
1.25-1.50	3	3	2	8
1.50-1.75	7	5	6	30
1.75-2.00	12	25	5	62
2.00-2.25	2	42	5	47
2.25-2.50	1	21	2	48
2.50-3.00	0	17	0	75

Table A.1: Number of entries in regions of data scatter plot

$W_{\gamma\gamma}$	$\alpha^1_{\rho\omega}$	$\alpha^2_{\rho\omega}$	$\alpha^3_{\rho\omega}$	$\alpha^4_{\rho\omega}$
1.25-1.50	.28	.20	.12	.40
1.50-1.75	.22	.09	.11	.58
1.75-2.00	.17	.18	.08	.57
2.00-2.25	.15	.19	.08	.58
2.25-2.50	.15	.20	.08	.57
2.50-3.00	.14	.16	.08	.62

Table A.2: Fraction of entries in various regions for $\rho^0\omega$ events

$W_{\gamma\gamma}$	$\alpha^1_{\rho 3\pi}$	$\alpha^2_{\rho 3\pi}$	$\alpha^3_{\rho 3\pi}$	$\alpha^4_{\rho 3\pi}$
1.25-1.50	.12	.33	.12	.43
1.50-1.75	.07	.20	.10	.63
1.75-2.00	.03	.42	.03	.53
2.00-2.25	.02	.48	.02	.49
2.25-2.50	.01	.48	.01	.50
2.50-3.00	0.0	.45	0.0	.55

Table A.3: Fraction of entries in various regions for $\rho 3\pi$ events

$W_{\gamma\gamma}$	$\alpha^1_{\omega 2\pi}$	$\alpha^2_{\omega 2\pi}$	$\alpha^3_{\omega 2\pi}$	$\alpha^4_{\omega 2\pi}$
1.25-1.50	.14	.21	.26	.39
1.50-1.75	.12	.09	.19	.60
1.75-2.00	.10	.19	.15	.56
2.00-2.25	.08	.17	.17	.58
2.25-2.50	.05	.19	.17	.59
2.50-3.00	.03	.15	.18	.64

Table A.4: Fraction of entries in various regions for $\omega 2\pi$ events

$W_{\gamma\gamma}$	$\alpha^1_{5\pi}$	$\alpha^2_{5\pi}$	$\alpha^3_{5\pi}$	$\alpha^4_{5\pi}$
1.25-1.50	.07	.26	.16	.51
1.50-1.75	.04	.16	.10	.70
1.75-2.00	.03	.25	.04	.68
2.00-2.25	.01	.32	.03	.64
2.25-2.50	.01	.32	.02	.65
2.50-3.00	0.0	.29	.01	.70

Table A.5: Fraction of entries in various regions for 5π events

$W_{\gamma\gamma}$	$f_{\rho\omega}$	$f_{\rho 3\pi}$	$f_{\omega 2\pi}$	$f_{5\pi}$
1.25-1.50	.56 (.38)	0.0 (.85)	0.0 (.73)	.44 (.39)
1.50-1.75	.49 (.34)	0.0 (1.0)	.24 (.62)	.27 (.35)
1.75-2.00	.56 (.19)	.18 (.22)	0.0 (.19)	.26 (.29)
2.00-2.25	0.0 (.11)	.81 (.24)	.19 (.10)	0.0 (.30)
2.25-2.50	.02 (.15)	0.0 (.26)	.05 (.16)	.93 (.16)
2.50-3.00	.06 (.05)	.20 (.09)	0.0 (.07)	.74 (.09)

Table A.6: Results of the 4 region fit

Table A.6 displays the fit fractions (and their errors, in parentheses) from the 4 region fit.

Table A.7 displays the results of the 2 region fit.

$W_{\gamma\gamma}$	f_{with}	$f_{without}$
1.25-1.50	.45 (.24)	.55 (.24)
1.50-1.75	.71 (.14)	.29 (.14)
1.75-2.00	.54 (.09)	.46 (.09)
2.00-2.25	.20 (.09)	.80 (.10)
2.25-2.50	.10 (.08)	.90 (.11)
2.50-3.00	.04 (.04)	.96 (.09)

Table A.7: Results of the 2 region fit

Bibliography

[1] F. Halzen and A. Martin. *Quarks and Leptons: an Introductory Course in Modern Particle Physics*, page 311. John Wiley and Sons, 1984.

[2] V.M. Budnev, et al. *Phys. Rep.* **15C**, 181 (1975).

[3] G. Bonneau, et al. *Nucl. Phys.* **B54**, 573 (1973).

[4] S. J. Brodsky, et al. *Phys. Rev.* **D4**, 1532 (1971).

[5] H. Kolanoski. *Two-photon Physics at e^+e^- Storage Rings.* Volume 105 of *Springer Tracts in Modern Physics*, 1984.

[6] F. Halzen and A. Martin. *Quarks and Leptons: an Introductory Course in Modern Particle Physics*, page 45. John Wiley and Sons, 1984.

[7] D. H. Perkins. *Introduction to High Energy Physics*, page 182. Addison-Wesley, 1982.

[8] J. J. Sakurai. *Phys. Rev. Lett.* **22**, 981 (1969).

[9] R. Brandelik, et al. *Phys. Lett.* **97B**, 448 (1980).

[10] P. M. Patel. First Observation of $\omega\rho^0$ and $K^{0*}\bar{K}^{0*}$ Production in $\gamma\gamma$ Collisions at ARGUS. In *Proceedings of the 23rd International Conference on High Energy Physics*, 1986.

[11] H. Aihara, et al. *Nucl. Instr. Meth.* **217**, 259 (1983).

[12] William W. Moses. *Measurement of the Inclusive Branching Fraction $\tau^- \rightarrow \nu_\tau \pi^- \pi^0 +$ neutral meson(s)*. PhD thesis, University of California, Berkeley, December 1986. LBL-22579.

[13] M. Wayne. *A Measurement of the Two-Photon Decay Width of the Eta Meson with the PEP4 Facility.* PhD thesis, University of California, Los Angeles, 1985. UCLA-85-010.

[14] J. William Gary. *Tests of Models for Parton Fragmentation in e^+e^- Annihilation.* PhD thesis, University of California, Berkeley, November 1985. LBL-20638.

[15] Mike Ronan. *The PEP4 (TPC) Trigger System.* Technical Report, TPC Report TPC-LBL-87-12, LBL, 1987.

[16] G. Gidal et al. *Major Detectors in Elementary Particle Physics.* Technical Report, Particle Data Group, LBL, 1985. Note: the calorimeter resolutions quoted are nominal, and differ from those used in this analysis.

[17] Marjorie D. Shapiro. *Inclusive Hadron Production and Two Particle Correlations in e^+e^- Annihilation at 29 GeV Center-of-Mass Energy.* PhD thesis, University of California, Berkeley, December 1984. LBL-18820.

[18] Mike Ronan. *The SelTwoGam Selection Process.* Technical Report, TPC Report TPC-LBL-87-15, LBL, 1987.

[19] O. I. Dahl et al. *SQUAW Kinematic Fitting Program.* Technical Report, Group A Programming Note P-126, LBL, 1968.

[20] Clark Lindsey. *Four Charged Particle Final States in Untagged Two-Photon Events at PEP.* PhD thesis, University of California, Riverside, August 1984.

[21] Gordon J. VanDalen. *FMC - Verlund User's Guide.* Technical Report, TPC Report TPC-UCR-84-1, LBL, 1984.

[22] Gordon J. VanDalen. p_T *Smearing in the Equivalent Photon Monte Carlo - TWOLUND.* Technical Report, TPC Report TPC-UCR-84-3, LBL, 1984.

[23] R. L. Ford and W. R. Nelson. *The EGS Code System: Computer Programs for the Monte Carlo Simulation of Electromagnetic Cascade Showers (Version 3).* Technical Report, SLAC Report SLAC-210, 1978.

[24] Mike Ronan. *The PEP4 (TPC) Trigger Monte Carlo.* Technical Report, TPC Report TPC-LBL-87-14, LBL, 1987.

[25] B. Gabioud. *Graphic and Interactive Minimization Program PEP4 MINUIT.* Technical Report, TPC Report TPC-LBL-83-41, LBL, 1983.

[26] Kevin Derby. *Integrated Luminosity for Experiments 14-18.* Technical Report, TPC Report TPC-LBL-87-17, LBL, 1987.

[27] H.-J. Behrend, et al. *Zeit. Phys.* **C21**, 205 (1984).

[28] D. L. Burke, et al. *Phys. Lett.* **103B**, 153 (1981).

[29] Adriaan Buijs. *Production of Four-Prong Final States in Photon-Photon Collisions.* PhD thesis, Rijks Universiteit Utrecht, March 1987.

[30] J. B. Dainton. Two Photon Physics. In *Proceedings of the International Europhysics Conference on High Energy Physics, Brighton*, 1983.

[31] Ch. Berger, et al. *Zeit. Phys.* **C29**, 183 (1985).

[32] J. Prentice. Plenary Session S-14. In *Proceedings of the International Europhysics Conference on High Energy Physics*, 1987.

[33] The ARGUS Collaboration. First Observation of $\gamma\gamma \rightarrow \omega\rho^0$. In *Proceedings of the International Europhysics Conference on High Energy Physics*, 1987.

[34] J. J. Sakurai. *Advanced Quantum Mechanics*, page 217. Addison-Wesley, 1967.

[35] G. Alexander, et al. *Phys. Rev.* **D26**, 1198 (1982).

[36] G. Alexander, et al. *Zeit. Phys.* **C30**, 65 (1986).

[37] R. J. Jaffe. *Phys. Rev.* **D15**, 267 (1977).

[38] R. J. Jaffe. *Phys. Rev.* **D15**, 281 (1977).

[39] N. N. Achasov et al. *Phys. Lett.* **108B**, 134 (1982).

[40] N. N. Achasov et al. *Zeit. Phys.* **C16**, 55 (1982).

[41] N. N. Achasov et al. *Zeit. Phys.* **C27**, 99 (1985).

[42] B.-A. Li and K.-F. Liu. *Phys. Lett.* **118B**, 435 (1982).

[43] B.-A. Li and K.-F. Liu. *Phys. Rev. Lett.* **51**, 1510 (1983).

LAWRENCE BERKELEY LABORATORY
TECHNICAL INFORMATION DEPARTMENT
UNIVERSITY OF CALIFORNIA
BERKELEY, CALIFORNIA 94720